npj | vaccines

Article

Published in partnership with the Sealy Institute for Vaccine Sciences

https://doi.org/10.1038/s41541-024-00961-6

Low-frequency CD8$^+$ T cells induced by SIGN-R1$^+$ macrophage-targeted vaccine confer SARS-CoV-2 clearance in mice

Daisuke Muraoka[1,2,11] ✉, Meng Ling Moi[3,4,11] ✉, Osamu Muto[5,6], Takaaki Nakatsukasa[1,7], Situo Deng[1], Chieko Takashima[2], Rui Yamaguchi[5,6], Shin-ichi Sawada[8], Haruka Hayakawa[3], Thi Thanh Ngan Nguyen[4], Yasunari Haseda[9], Takatoshi Soga[9], Hirokazu Matsushita[2], Hiroaki Ikeda[1], Kazunari Akiyoshi[10] & Naozumi Harada[9]

Vaccine-induced T cells and neutralizing antibodies are essential for protection against SARS-CoV-2. Previously, we demonstrated that an antigen delivery system, pullulan nanogel (PNG), delivers vaccine antigen to lymph node medullary macrophages and thereby enhances the induction of specific CD8$^+$ T cells. In this study, we revealed that medullary macrophage-selective delivery by PNG depends on its binding to a C-type lectin SIGN-R1. In a K18-hACE2 mouse model of SARS-CoV-2 infection, vaccination with a PNG-encapsulated receptor-binding domain of spike protein decreased the viral load and prolonged the survival in the CD8$^+$ T cell- and B cell-dependent manners. T cell receptor repertoire analysis revealed that although the vaccine induced T cells at various frequencies, low-frequency specific T cells mainly promoted virus clearance. Thus, the induction of specific CD8$^+$ T cells that respond quickly to viral infection, even at low frequencies, is important for vaccine efficacy and can be achieved by SIGN-R1$^+$ medullary macrophage-targeted antigen delivery.

The number of cases of the coronavirus disease 2019 (COVID-19) caused by severe acute respiratory syndrome coronavirus 2 (SARS-CoV-2) has surpassed 77 million worldwide, with a mortality of more than 7 million (https://covid19.who.int/)[1–3]. Vaccination plays a vital role in controlling the global spread of COVID-19 by mounting immune responses against the virus[4–8].

The spike (S) protein of SARS-CoV-2, particularly its receptor-binding domain (RBD), is a key target for neutralizing antibodies that inhibit the binding of the S protein to its receptor, ACE2 on host cells, thereby preventing infection[9–12]. Almost all SARS-CoV-2 vaccines contain the whole S protein or RBD as an antigen for the induction of neutralizing antibodies. Various types of vaccines have been developed, including inactivated virus, DNA, mRNA, and protein vaccines. To date, mRNA, protein, inactivated virus, and viral vector vaccines have been approved for use worldwide[4,8]; however, the virus has acquired several mutations that enable the evasion from vaccine-induced immune responses. The most number of mutations of concern are those located in the S protein that cause a reduction in its binding affinity to neutralizing antibodies[13–26]. Thus, vaccine platforms that exclusively rely on the induction of neutralizing antibodies may have limited efficacy against some variants of SARS-CoV-2 and may, in turn, drive the emergence of strains that are resistant to neutralization. In addition, the durability of the humoral response to SARS-CoV-2 was reported to be limited to a few months[27], and the plasma levels of S1 protein-specific neutralizing antibodies were not detected in several patients who had recovered from COVID-19[28], indicating that the neutralizing antibodies likely only provide short-term protection.

The SARS-CoV-2-specific CD8$^+$ T cell response is a key mechanism for the prevention of SARS-CoV-2 infection[29,30]. Patients with virus-specific CD8$^+$ T cells in the acute phase have a better prognosis after infection, implying that CD8$^+$ T cells contribute to the control of

[1]Department of Oncology, Nagasaki University Graduate School of Biomedical Sciences, Nagasaki, Japan. [2]Division of Translational Oncoimmunology, Aichi Cancer Center Research Institute, Nagoya, Japan. [3]School of International Health, Graduate School of Medicine, the University of Tokyo, Tokyo, Japan. [4]Institute of Tropical Medicine, Nagasaki University, Nagasaki, Japan. [5]Division of Cancer Systems Biology, Aichi Cancer Center Research Institute, Nagoya, Japan. [6]Division of Cancer Informatics, Nagoya University Graduate School of Medicine, Nagoya, Japan. [7]Department of Surgical Oncology, Nagasaki University Graduate School of Biomedical Sciences, Nagasaki, Japan. [8]Synergy Institute for Futuristic Mucosal Vaccine Research and Development (cSIMVa), Chiba University, Chiba, Japan. [9]United Immunity, Co., Ltd., Tokyo, 103-0022, Japan. [10]Department of Immunology, Graduate School of Medicine, Kyoto University, Kyoto, Japan. [11]These authors contributed equally: Daisuke Muraoka, Meng Ling Moi. ✉e-mail: d.muraoka@aichi-cc.jp; sherry@m.u-tokyo.ac.jp

SARS-CoV-2 infection[31]. Additionally, clearance of SARS-CoV-2 by vaccines is mediated by virus-specific $CD8^+$ T cells[32,33]. Interestingly, vaccination against the nucleocapsid (N) protein in cynomolgus macaques did not induce virus neutralization antibodies but prevented SARS-CoV-2 infection[33]. In a mouse model, vaccination against the N protein alone elicited cellular immune responses that could control SARS-CoV-2[34], and a combined N- and S-protein vaccine had better efficacy against SARS-CoV-2 infection than the S vaccine alone[34,35].

The vaccine-induced SARS-CoV-2-specific $CD8^+$ T cell response likely has a key role in virus clearance and urgent investigation is required to elucidate its underlying mechanism to enable the development of effective long-term vaccines. As an efficient $CD8^+$ T cell-inducing vaccine, we generated a nanoparticulate RBD protein vaccine utilizing the pullulan nanogel (PNG) antigen delivery system. Nanogel is a nanoparticulate hydrogel with three-dimensional crosslinked polymer networks. Nanogel has recently attracted attention as nanocarriers for drug delivery[36,37]. Cholesteryl pullulan, a pullulan polysaccharide modified with cholesterol, automatically forms a nanogel through hydrophobic interactions between cholesterol groups. The resulting PNG can efficiently encapsulate proteins and peptides into its polymer network, thereby solubilizing and stabilizing these cargos. We previously reported that, when subcutaneously injected into mice, a peptide antigen-loaded PNG migrates to the draining lymph node (DLN) in a cell-independent manner, where it is engulfed by antigen-presenting cells, especially medullary macrophages, which can exert efficient cross-presentation activity in the presence of Toll-like receptor (TLR) stimulation, resulting in the induction of a strong $CD8^+$ T cell response[38–40]. PNG has been tested as a vaccine delivery system in a series of clinical trials[41–44].

In this study, using a PNG-encapsulated S RBD protein vaccine (PNG:RBD vaccine), we investigated how virus-specific $CD8^+$ T cells and antibodies contribute to the clearance of SARS-CoV-2 after vaccination. First, we confirmed that the PNG:RBD vaccine could induce a strong RBD-specific $CD8^+$ T cell response in the vaccinated healthy mice. Simultaneously, we identified mouse C-type lectin SIGN-R1 (CD209b) as a physiological receptor for PNG, which explains lymph node medullary macrophage-selective antigen delivery and enhanced $CD8^+$ T cell induction. We investigated how RBD-specific $CD8^+$ T cells and antibodies contribute to the clearance of SARS-CoV-2 after vaccination with the PNG:RBD vaccine. The vaccine efficiently prevented SARS-CoV-2 infection in a K18-hACE2 mouse model, which required both $CD8^+$ T cells and B cells. Furthermore, computational analysis of T cell receptor (TCR)-sequence data revealed that vaccine-mediated virus clearance was primarily mediated by $CD8^+$ T cells induced at a very low frequency, rather than at a high frequency. Our study suggests that the induction of low-frequency virus-specific $CD8^+$ T cell clones that expand rapidly after infection is crucial in determining vaccine efficacy, compared to those that induce monoclonal virus-specific $CD8^+$ T cells.

Results

Medullary macrophage-selective antigen delivery by PNG depends on binding to SIGN-R1

We previously demonstrated that the nanoparticulate vaccine-delivery system PNG delivered vaccine antigens to lymph node medullary macrophages after subcutaneous injection and strongly enhanced antigen-specific $CD8^+$ T cell responses through cross-presentation by medullary macrophages[39]. However, the mechanism underlying medullary macrophage-selective antigen delivery by PNG remains unclear. Given that pullulan, the backbone of PNG, is a polysaccharide and that antigen-presenting cells, such as macrophages and dendritic cells, express C-type lectins to recognize polysaccharides on pathogens, we first investigated whether PNG binds to mouse C-type lectins expressed in HeLa cells, including DC-SIGN (CD209a), SIGN-R1 (CD209b), mannose receptor (MRC, CD206), Dectin-1 (CD369), and macrophage-inducible C-type lectin (Mincle, CD200). PNG was found to predominantly bind to SIGN-R1 (Fig. 1a, b), and is occluded by anti-SIGN-R1 antibody (Fig. 1b). PNG did not bind to SIGN-R1 lacking the carbohydrate-recognition (CRD) domain (Fig. 1c). In previous studies, we have shown that subcutaneously injected PNG is engulfed by medullary macrophages[39], and therefore, we examined whether this uptake of PNG by medullary macrophages is mediated by SIGN-R1. First, we investigated whether medullary macrophages express SIGN-R1 and found that both medullary sinus macrophages (MSMs) and medullary cord macrophages (MCMs) express SIGN-R1, consistent with previous reports[45] (Fig. 1d). Additionally, when subcutaneously injected into mice, PNG was efficiently engulfed by these medullary macrophages in the DLN, and this uptake was significantly blocked by the administration of anti-SIGN-R1 antibody (Fig. 1e, f). Next, we examined whether this antigen uptake mediated by SIGN-R1 enhances antigen presentation by medullary macrophages utilizing a PNG:long peptide antigen complex used in our previous study[39]. This showed that antigen presentation was attenuated by anti-SIGN-R1 antibody (Supplementary Fig. 1). These results clearly indicate that PNG can deliver antigens to medullary macrophages predominance by selectively binding to SIGN-R1 which promotes antigen presentation by medullary macrophages.

PNG-encapsulated RBD vaccine effectively prevents SARS-CoV-2 infection by inducing a potent $CD8^+$ T cell response in mice

We investigated whether PNG vaccine induces cellular immunity via SIGN-$R1^+$ medullary macrophages and evaluated its effects on the $CD8^+$ T cell response to virus infection using the PNG:RBD vaccine (Supplementary Fig. 2a). The PNG:RBD vaccine had a diameter of 54.2 nm (Supplementary Fig. 2b). Efficient encapsulation was confirmed using size exclusion high performance liquid chromatography (SE-HPLC, Supplementary Fig. 2c). The PNG:RBD vaccine induced RBD-specific $CD8^+$ T cell responses, which were attenuated by using anti-SIGN-R1 antibody (Supplementary Fig. 3). Next, we evaluated the immunogenicity of PNG:RBD vaccine comparing to that of the RBD alone vaccine. Consistent with our previous result using a different vaccine antigen[39], the PNG:RBD vaccine induced significantly higher RBD-specific $CD8^+$ T cell responses compared to those with the RBD alone vaccine after one or two vaccinations (Fig. 2a). Even 3 weeks after the last immunization, greater RBD-specific $CD8^+$ T cell responses were detected in the spleens and lungs of the PNG:RBD vaccine group than those in the RBD alone vaccine group (Fig. 2a, b). These RBD-specific $CD8^+$ T cells included abundant effector T cells ($CD44^+CCR7^-CD127^-$) and effector memory T cells ($CD44^+CCR7^-CD127^+$) and were induced in both the PNG:RBD and RBD alone vaccine groups (Fig. 2c, d, f, g). Low CD45RB and high KLRG expression was previously reported to correlate with high TCR affinity and effector function[46]. In the PNG:RBD vaccine group, the expression of KLRG was higher than that in the RBD alone vaccine group (Figs. 2e, h). Additionally in the PNG:RBD vaccine group, the CD45RB expression in effector memory T cells was lower than in the control group, but not in the RBD alone vaccine group (Figs. 2e, h). These findings suggest that the PNG:RBD vaccine efficiently induced antigen-specific memory $CD8^+$ T cells with high antigen recognition ability and effector function. However, the induction of RBD-specific $CD4^+$ T cell responses was comparable between the RBD alone and PNG:RBD vaccines and there was also no differences in the phenotypes and the expression of the activation markers CD137 and CD69 of $CD4^+$ T cells between these vaccines in the lungs and spleens (Supplementary Fig. 4). Regarding vaccine-induced humoral responses, although the PNG:RBD vaccine induced humoral immune responses, there were no significant differences in the titer of RBD-specific serum IgG antibodies between the PNG:RBD and RBD alone vaccine groups (Fig. 2i and Supplementary Fig. 5). Neutralizing antibodies were induced in both groups to a similar degree, as assessed by antibody-mediated inhibition of RBD and hACE2 protein binding (Fig. 2j).

We evaluated the efficacy of the PNG:RBD vaccine in protecting against SARS-CoV-2 in a K18-hACE2 transgenic mouse model[47]. Intranasal dosing of SARS-CoV-2 at 5×10^4 plaque-forming units (PFU) resulted in a 100% death rate in the control group (Fig. 3a). Two of seven (28.6%) mice in the RBD alone vaccine group died, whereas all mice in the PNG:RBD vaccine group survived. Furthermore, we found that although SARS-CoV-2 infection decreased the body weight by 20% in the control group, PNG:RBD

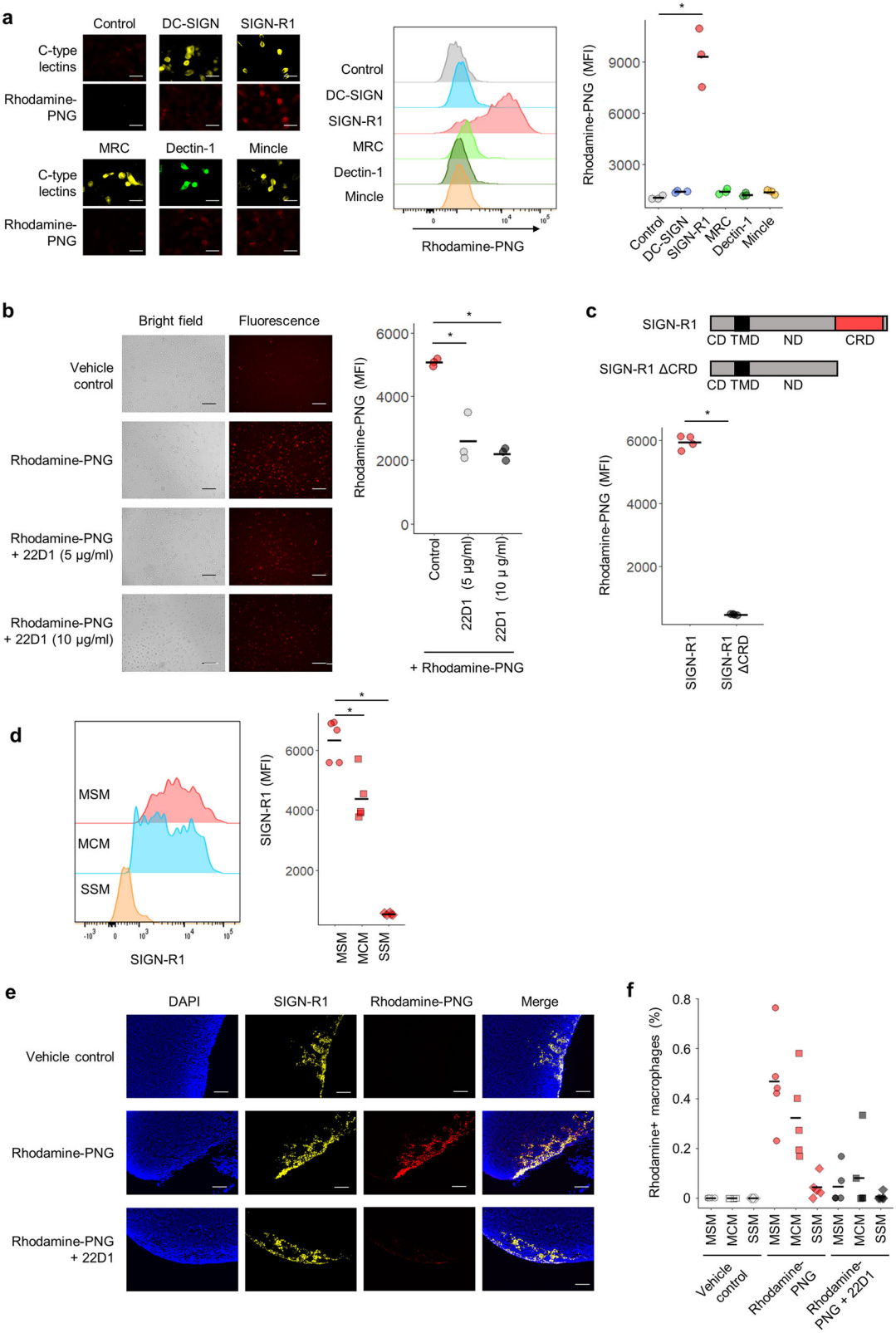

Fig. 1 | PNG-based vaccine delivery system specifically binds to mouse SIGN-R1. **a**, **b**, **c** HeLa cells were transduced with cDNA encoding the indicated C-type lectin receptor and incubated with rhodamine-PNG for 30 min. The rhodamine signal was observed under a microscope or detected by flow cytometry (scale bar = 50 μm). **b** Anti-SIGN-R1 antibody (22D1) was added to the cells 60 min prior to the addition of PNG (scale bar = 100 μm). **d** SIGN-R1 expression in macrophages were examined by flow cytometry. **e**, **f** Rhodamine-PNG was subcutaneously administrated into normal mice and the inguinal lymph node was collected after 10 min (scale bar = 100 μm). The rhodamine signal was observed by microscopy (**d**) or detected by flow cytometry (**e**). Anti-SIGN-R1 antibody (22D1) was subcutaneously injected into mice for blocking 60 min prior to the injection of PNG. *$p < 0.05$; n.s., not significant.

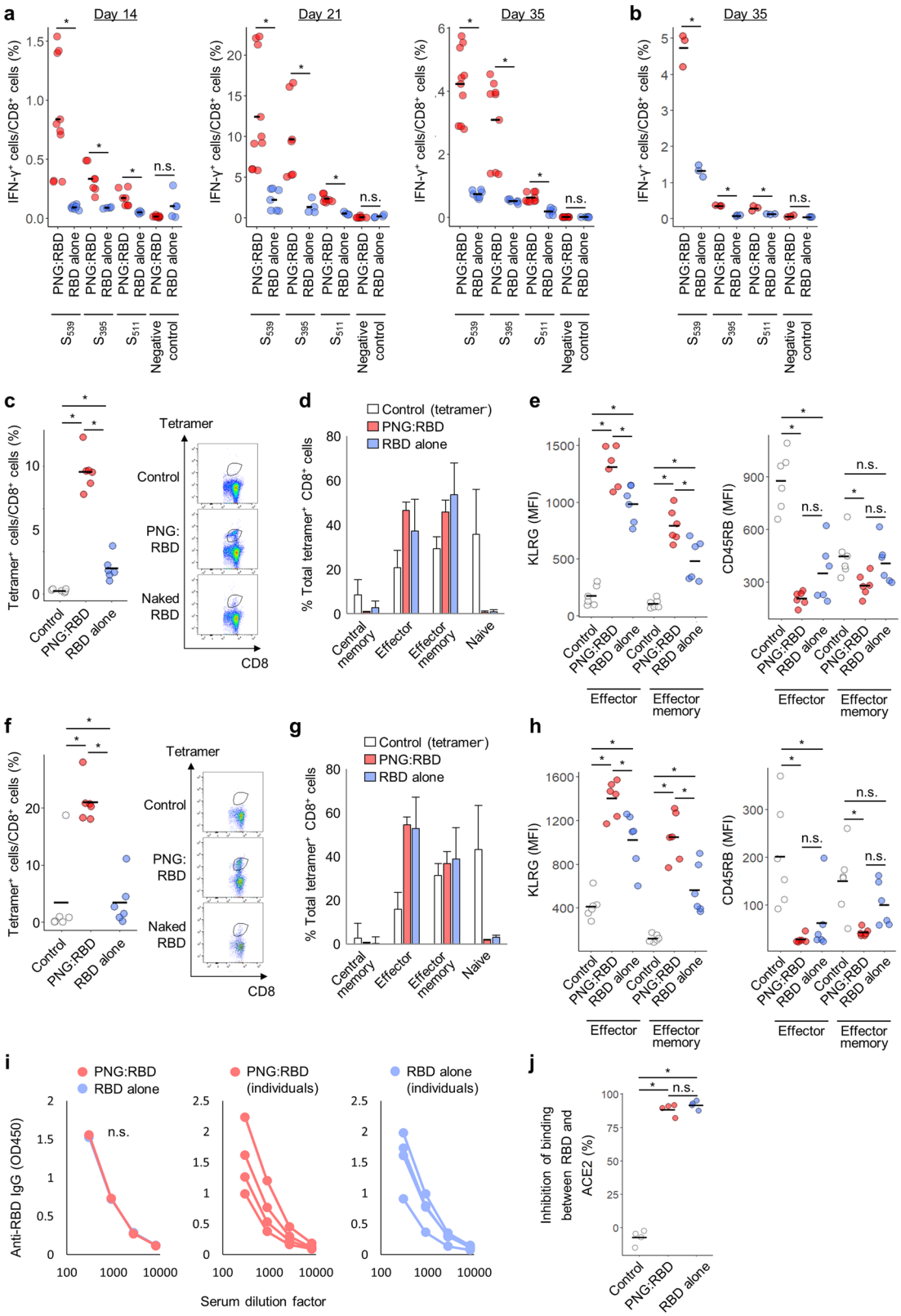

Fig. 2 | PNG:RBD vaccine induces strong cellular and humoral immune responses against SARS-CoV-2 S RBD in mice. K18-hACE2 mice were immunized with the PNG:RBD or RBD alone vaccine twice at a 2-week interval. (**a**) Spleens or (**b**) lungs were obtained on the indicated days and specific T cell induction was analyzed with an intracellular cytokine staining assay using stimulation with the indicated peptides. **c**–**h** Characteristics of RBD-specific $CD8^+$ T cells from the spleen (**c**–**e**) or lung (**f**–**h**). **i** Binding of total serum IgG to the RBD protein. Serum was obtained from vaccinated mice on day 35. Data represent OD 450 nm values for each group of four mice. **j** Serum was collected on day 35 and the inhibition of binding between RBD and hACE2 proteins was assessed. $^*p < 0.05$; n.s., not significant.

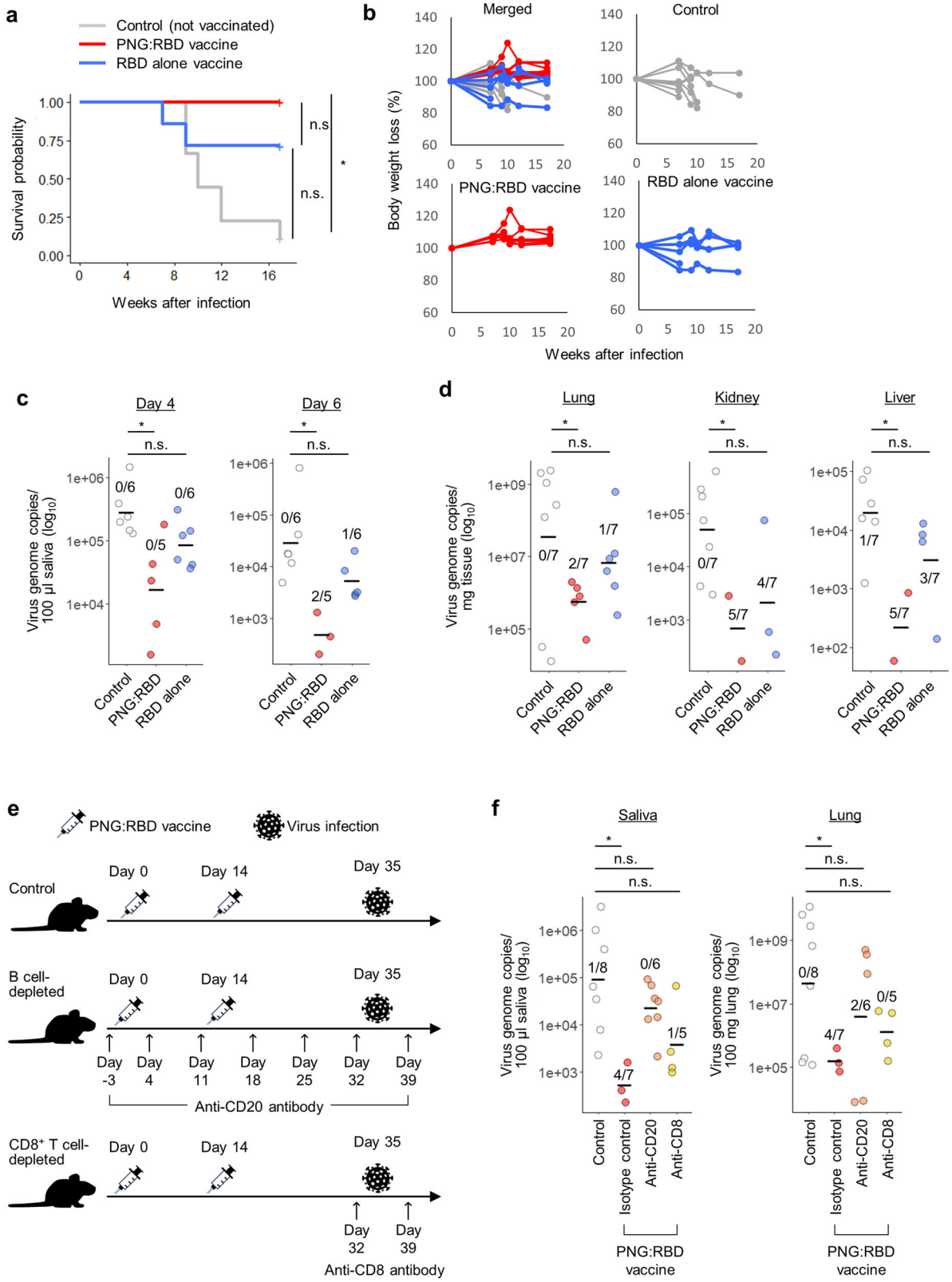

Fig. 3 | PNG:RBD vaccine induced better protective immunity to SARS-CoV-2 in the CD8$^+$ T cell- and B cell-dependent manners. K18-hACE2 mice were immunized with the PNG:RBD or RBD alone vaccine twice at a 2-week interval. At 21 days after the 2nd vaccination, mice were challenged with SARS-CoV-2. **a** Kaplan–Meier survival curve over 17 days post viral infection. **b** Body weight changes in mice after SARS-CoV-2 infection. **c**, **d** Saliva, lungs, kidneys, and livers were collected at 4 or 6 days post infection. Viral RNA was measured using quantitative PCR. **e** Experimental design for investigating the cells responsible for protecting from immune protection against SARS-CoV-2 in K18-hACE2 mice. **f** Mice were intraperitoneally injected with anti-mouse CD8a or anti-mouse CD20 antibody prior to infection and post infection. Saliva and lungs were collected at 6 days post infection and quantitative PCR was performed to measure viral RNA. Data are presented as mean ± SD. *$p < 0.05$; n.s., not significant.

prevented this weight loss. On the other hand, in the RBD alone vaccine group, a decrease in body weight was observed in some mice (Fig. 3b). Next, we evaluated the virus titers in the appropriate organs after vaccination in the infected hACE2 mice. As infection was not detected in the spleen, virus titers were measured in the saliva, lung, kidney, and liver (Supplementary Fig. 6). At 4 or 6 days post-virus challenge, although the viral titer was reduced in the saliva in mice vaccinated with RBD alone, this decrease was not significant compared to the reduction in the control group. On the other hand, PNG:RBD vaccine significantly reduced viral titers in the saliva when compared to the control group (Fig. 3c). Similarly, the virus titers in the lungs, kidneys, and livers of the PNG:RBD vaccine group were also significantly lower than those in the control or RBD alone vaccine groups (Fig. 3d). To understand the contribution of T and B cells to PNG:RBD vaccine-mediated virus clearance, we examined the virus titer in the $CD8^+$ T cell- or B cell-depleted hACE2 mice (Fig. 3e). $CD8^+$ T cells or B cells were depleted by administration of anti-CD8 and anti-CD20 antibodies, respectively; however, B cell depletion reduced the RBD-specific IgG while $CD8^+$ T cell depletion did not (Supplementary Fig. 7). Administration of these antibodies prior to virus infection reversed the virus titer in the saliva and lungs of the vaccinated mice, resulting in a higher number of mice in which the virus was detected (Fig. 3f). These results indicate that while the RBD alone vaccine does not clear SARS-CoV-2 well, the PNG:RBD vaccine could induce both virus specific antibody by B cells and antigen-specific $CD8^+$ T cells and their synergistic effect leads to the effective prevention of SARS-CoV-2 infection.

PNG:RBD vaccine rapidly blocks the upregulation of virus-induced genes

The effects of vaccination and/or infection on gene expression were examined in the relevant organs. We focused on the lungs, the main entry point of SARS-CoV-2 into the body and the frontline of defense against viral infection, and the spleen, an important lymphoid organ for immune induction. We performed whole-gene expression analysis in the organs of vaccinated or control mice on day 3 post infection to reveal the mechanism underlying virus clearance by the PNG:RBD vaccine. The experiment involved four groups of mice: "not vaccinated–not infected (control)," "not vaccinated–infected," "vaccinated–not infected," and "vaccinated–infected" mice (Fig. 4). Compared to the control group, the expression of multiple genes in the not vaccinated–infected group was significantly upregulated, while a few genes were predominantly downregulated (Fig. 4a). Gene ontology (GO) analysis in the not vaccinated–infected group revealed that the upregulated genes were related to the immune response against the virus, for example, Irf7 and Stat1, and interferon-stimulated genes, such as Isg15, Ifit1, Ifit3, Ifit3b, and Oasl2 (Fig. 4b and d). This suggests that virus infection rapidly induces the expression of virus response genes in the lungs. In addition, the virus response genes expression was higher in the not vaccinated–infected group than the vaccinated–infected group (Fig. 4c, e), and the expression of these genes was comparable between the control and vaccinated–infected groups (Supplementary Fig. 8). Virus-induced gene expression was also observed in the spleen, but was suppressed by the PNG:RBD vaccine (Supplementary Fig. 9). These data suggest that the PNG:RBD vaccine-induced immunity rapidly eliminates the virus before a strong virus-specific response is elicited. We performed a CIBERSORTx analysis to estimate the relative abundance of immune cells in a sample using gene expression data and thereby examine the effects of the PNG:RBD vaccine on immune cells in the SARS-CoV-2-infected mice. There were no significant differences in the proportion of $CD4^+$ T, $CD8^+$ T, and B cells in the lungs among the four groups (Fig. 5). However, the infection induced the polarization of $CD4^+$ T cells to Th1 phenotype. Interestingly, the PNG:RBD vaccine diminished this Th1-skewing effect. No significant changes in the proportion of other immune cells were observed after infection or vaccination (Supplementary Fig. 10). Additionally, we examined the active state of NK cells by using flow cytometry, as they have been reported to be involved in the clearance of SARS-CoV-2[48], but no significant differences were observed (Supplementary Fig. 11). Similar changes were observed in the spleen (Supplementary Figs. 12 and 13). Changes in cytokine expression by infection were also attenuated by the PNG:RBD vaccine (Fig. 4). These findings suggest that the rapid vaccine-mediated elimination of SARS-CoV-2 diminished the virus-induced changes in immune cell responses, such as Th1 polarization of $CD4^+$ T cells.

PNG:RBD vaccine induces specific $CD8^+$ T cell clones at low frequency that rapidly expand during virus infection

Since the prevention of virus infection by the PNG:RBD vaccine was dependent on $CD8^+$ T cells (Fig. 3e), we examined the TCR repertoires in the lung and spleen after vaccination or viral infection in naïve mice. The PNG:RBD vaccine significantly increased the frequency of the top 10 clones and reduced the diversity index score (inverse Simpson's index) in the lungs and spleens of naïve K18-hACE2 mice (Fig. 6a, b). Similar changes were observed in the infected mice (Fig. 6a, b). These findings suggest that, in naïve mice, both the PNG:RBD vaccine and virus infection predominantly induced the clonal expansion of antigen-specific T cells. Clonal expansion after PNG:RBD vaccination or viral infection was investigated in the lungs and spleens of each mouse by calculating the correlation coefficient of TCRβ CDR3. PNG:RBD vaccination significantly increased the correlation coefficient of TCRβ CDR3 between the spleen and lung compared to that in the control group, while viral infection had no effect (Fig. 6c, d). These results suggest that the vaccine induces T cells that are systemically distributed in vivo, whereas SARS-CoV-2 independently induces clonal T cell expansion in the lung and spleen. On the other hands, though the RBD alone vaccine induced the clonal expansion of antigen-specific T cells, these expansions were weak, and the change in the correlation coefficient of TCRβ CDR3 between the spleen and lung in the RBD alone vaccine group was slight (Supplementary Fig. 14a–d). These data are consistent with the data regarding RBD-specific $CD8^+$ T cells in Fig. 2, showing that the RBD alone vaccine could not induce a strong cellular immune response against the vaccine antigen. Next, we investigated the effect of virus infection on the TCR repertoire in the vaccinated mice. We expected a greater increase in T cell clonality as the antigen-specific T cells induced by the PNG:RBD vaccine further proliferated after viral infection; unexpectedly, virus infection mitigated the increase in the proportion of the top 10 TCRs and decrease in the inverse Simpson's index observed in the vaccinated mice (Fig. 6a, b). Furthermore, virus infection also significantly reduced the strong vaccine-induced correlation coefficient of TCRβ CDR3 between the lung and spleen (Fig. 6c, d). These findings suggest that viral infection in the vaccinated mice increases TCR diversity.

We examined why virus infection increased TCR diversity even in the PNG:RBD vaccinated mice. Because specific $CD8^+$ T cells contribute to the clearance of infected host cells during viral infection, we hypothesized that the observed change in TCR diversity by virus infection in the vaccinated mice was caused by the increase in the number of expanded specific $CD8^+$ T cells. Given that TCRs with similar CDR3 can recognize the same antigens[49], the enriched TCR clonotypes (meta-clonotypes enriched by vaccine or viral infection) are considered to be T cells specific for the respective antigens (i.e., virus or vaccine antigens)[50]. Additionally, since the PNG:RBD vaccine could not induce vaccine-specific $CD4^+$ T cells (Supplementary Fig. 4), we assumed that the change in TCR diversity in the vaccinated mice was derived from antigen-specific $CD8^+$ T cells. Therefore, we considered that changes in the meta-clonotypes reflects changes in antigen-specific $CD8^+$ T cells. First, to examine the changes in clonal expanded $CD8^+$ T cells, we evaluated the meta-clonotypes among the TCRs with 32 or more copies. Two meta-clonotypes were detected in both the lung and spleen of every vaccinated mouse (Fig. 6e and Table 1). Interestingly, virus infection increased the number of meta-clonotypes to seven and four in in the lungs and spleens, respectively, of the PNG:RBD vaccinated mice (Fig. 6e and Table 1). In contrast, only one meta-clonotype (with the centroid sequence CASSQDWGGYAEQFF) was detected in the lungs of unvaccinated mice, and no meta-clonotypes were detected in the spleens, even after virus infection (Fig. 6e and Table 1). Next, to examine

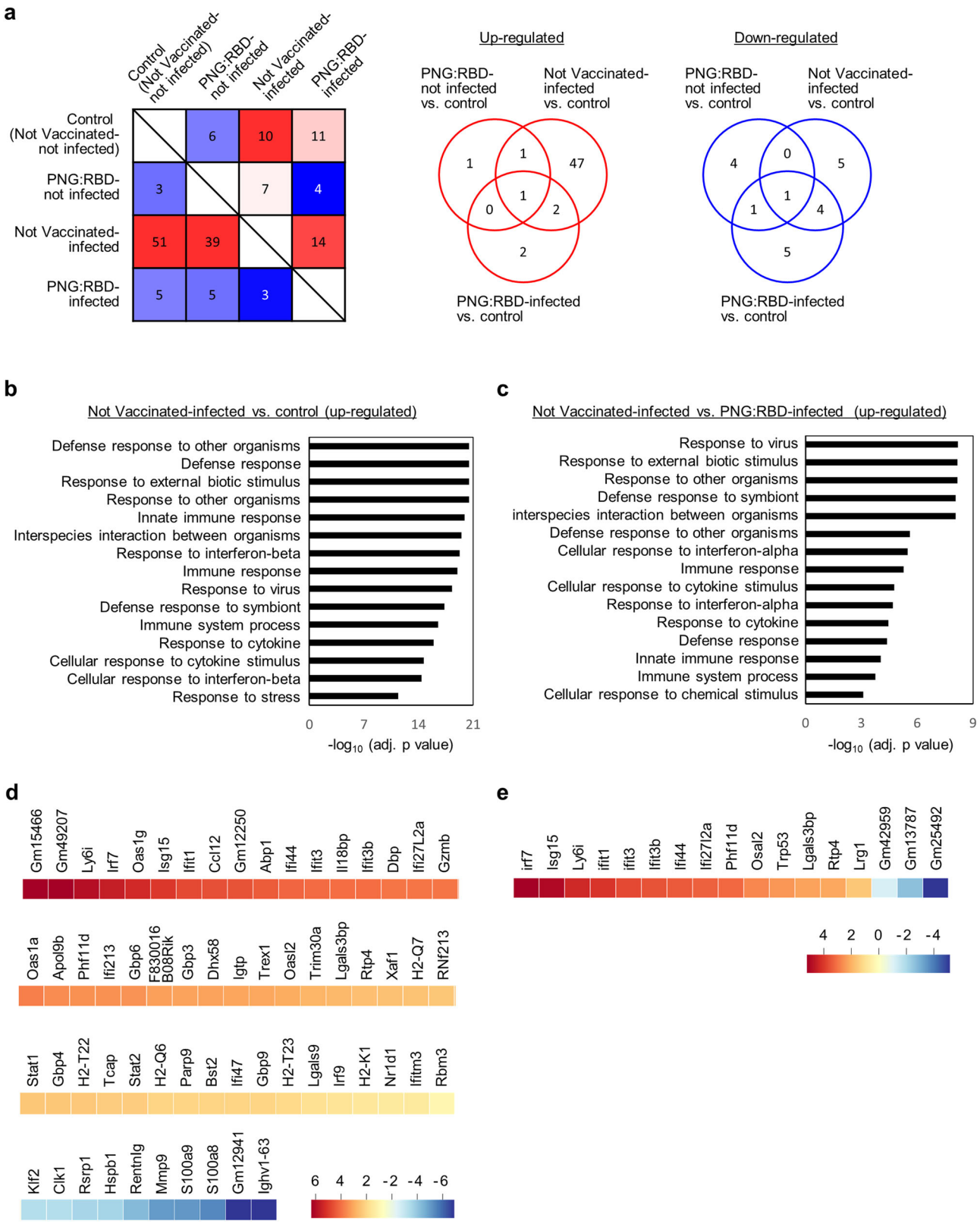

Fig. 4 | PNG:RBD vaccine blunted inflammation-related gene expression associating virus infection. K18-hACE2 mice were immunized with the PNG:RBD vaccine twice at a 2-week interval. At 21 days after the 2nd vaccination, mice were challenged with SARS-CoV-2. The lungs and spleens were collected 3 days post infection, and their RNA was subjected to RNA-seq analysis (3 mice in each group). **a** Venn diagram of overlapping genes identified in the differential expression analysis comparing the control, vaccinated–uninfected, not vaccinated–infected, and vaccinated–infected groups. **b**, **c** Gene ontology (GO) enrichment analysis of biological process terms enriched in the upregulated genes, comparing the not vaccinated–infected group with the control (**b**) or vaccinated–infected group (**c**). Heatmap representation of the average levels of genes upregulated in the not vaccinated–infected group compared with the control (**d**) or vaccinated–infected group (**e**).

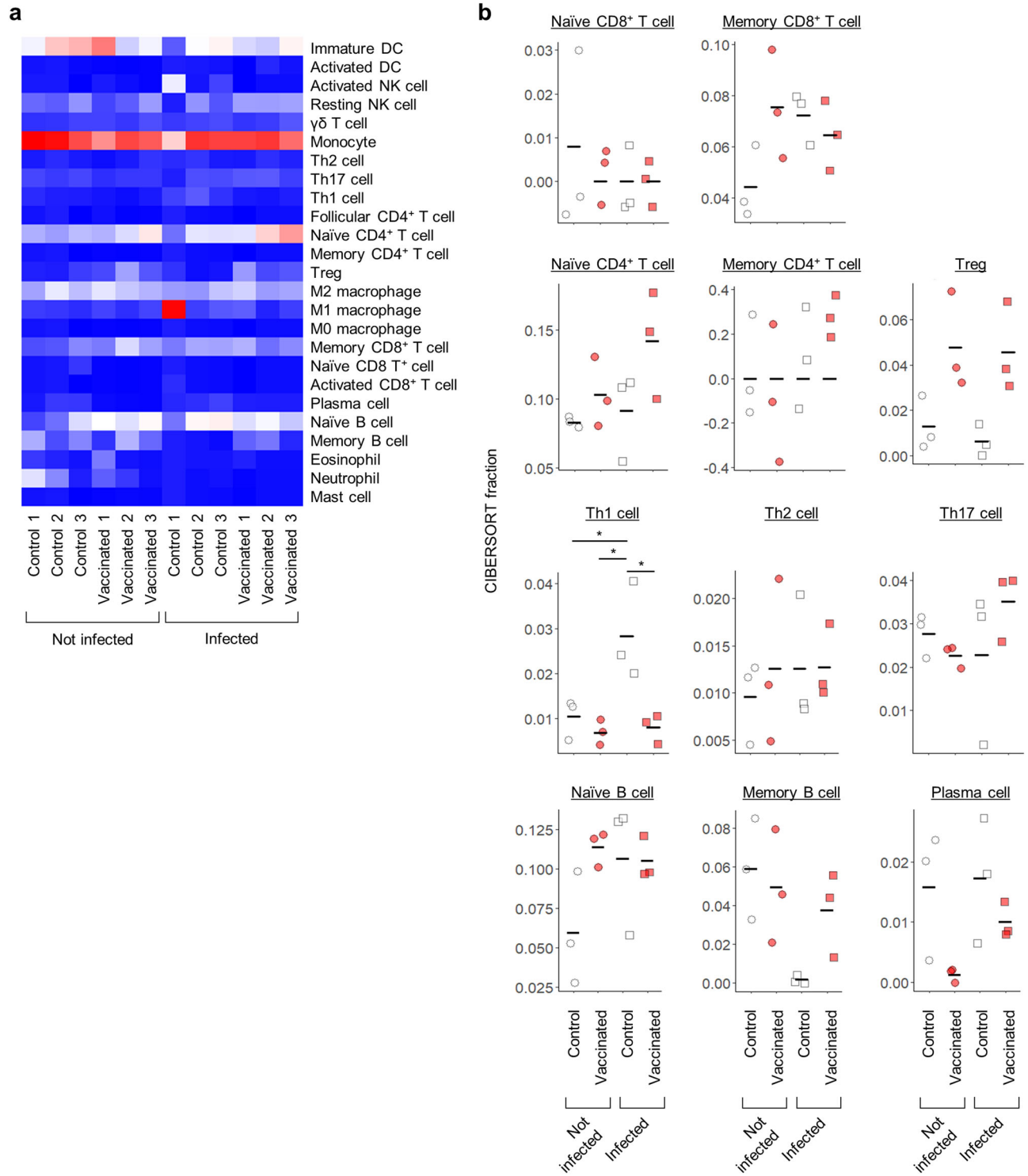

Fig. 5 | PNG:RBD vaccine suppressed changes in immune cell population after virus infection. K18-hACE2 mice were immunized with the PNG:RBD vaccine twice at a 2-week interval. At 21 days after the 2nd vaccination, mice were challenged with SARS-CoV-2. The lungs were collected 3 days post infection and RNA-seq was performed ($n = 3$ per group). RNA-seq data were subjected to CIBERSORTx analysis. Heatmap (**a**) and T cell and B cell infiltration patterns (**b**) are shown. *$p < 0.05$.

whether meta-clonotypes detected after viral infection were already induced even at low frequency by the PNG:RBD vaccination, we again evaluated the meta-clonotypes among all TCRs, including TCRs on unexpanded T cells that contained one or more TCR copies. We defined the clonotypes in meta-clonotypes 1 to 7 detected in the lungs of vaccinated–infected mice as "the meta-clonotype conformant TCRs" (Table 1). Then, we searched the TCR repertoire, including low-frequency TCRs in other groups, of the meta-clonotype conformant TCRs. Although there was variation between individual mice, all meta-clonotypes excluding the meta-clonotype 7 conformant TCRs were detected in the lungs or spleens of vaccinated mice (Fig. 6f). In contrast, although a few meta-clonotypes were detected in unvaccinated mice, the frequency was lower than that in vaccinated mice (Fig. 6f). Similar results for a lower frequency of these meta-clonotypes were obtained in the RBD alone vaccinated mice (Supplementary Fig. 14e). Next, we compared the read counts of clonotypes for all seven meta-clonotypes

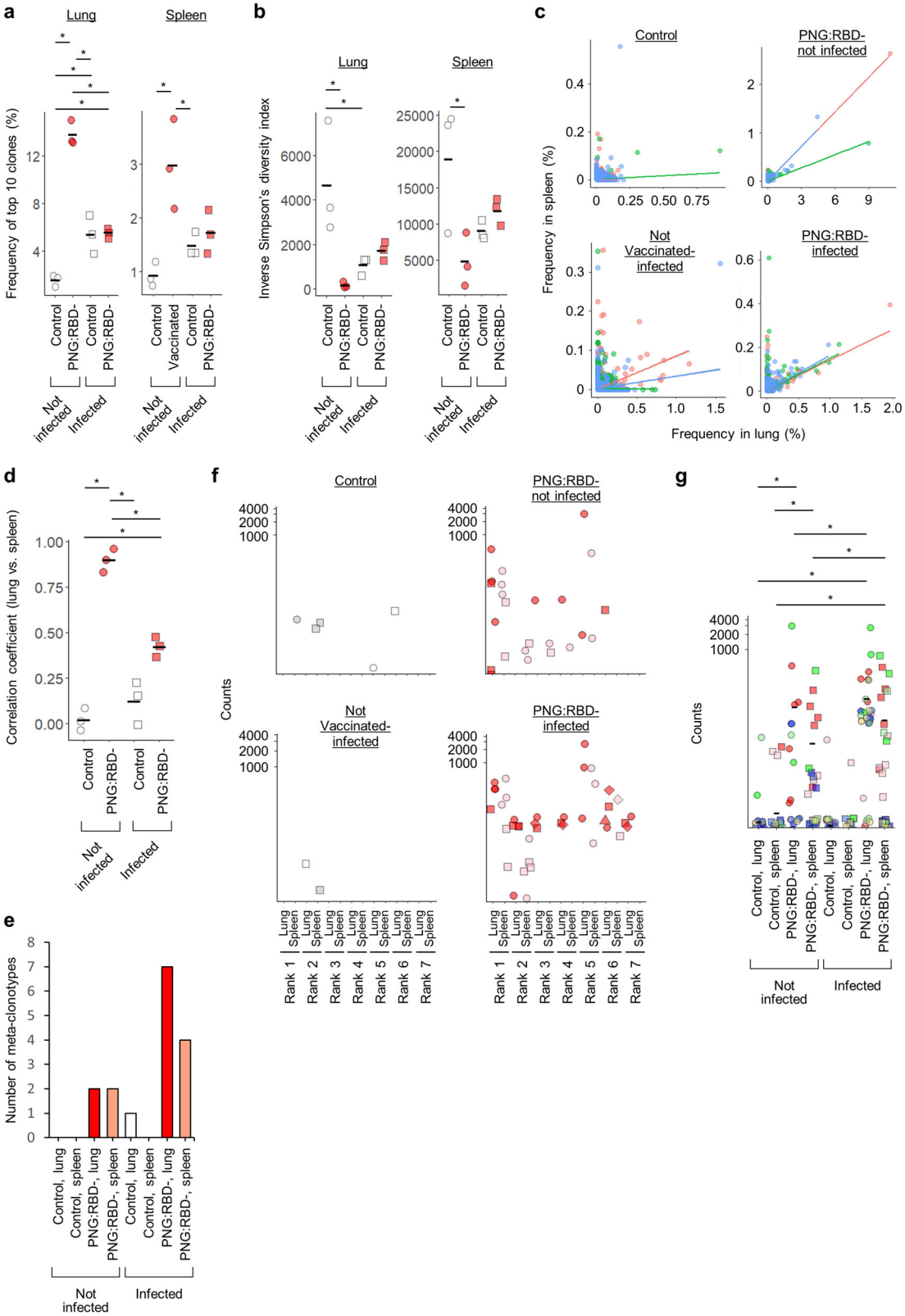

Fig. 6 | PNG:RBD induce the low-frequency T cells which clonal expanded after virus infection. K18-hACE2 mice were immunized with the PNG:RBD vaccine twice at a 2-week interval. At 21 days after the 2nd vaccination, mice were challenged with SARS-CoV-2. The lungs and spleens were collected 3 days post infection and TCR repertoire analysis was performed ($n = 3$ per group). Frequency of the top ten clones (**a**) and (**b**) inverse Simpson's diversity index in the lungs and spleens ($n = 3$ per group) was used to assess the diversity of TCR repertoires for each sample. **c**, **d** Correlation of the frequency of each T cell clone between the lungs and spleens ($n = 3$ per group). **e** Number of each meta-clonotype in the lungs and spleens ($n = 3$ per group). **f** Counts of meta-clonotypes detected in the lungs of vaccinated–infected mice. Each symbol represents three individual mice in each group. **g** Counts of meta-clonotypes detected in the lungs of vaccinated–infected mice. Each symbol represents an individual mouse, and the different colors represent 21 individual CDR3 clones. $^*p < 0.05$.

Table 1 | List of identified meta-clonotypes

Treatment	Virus	Organ	Centroids cdr3_b_aa	CDR3 motif	Enriched clonotypes	v_b_gene	j_b_gene
PNG:RBD	-	Lung	CASSLNNNERLFF	(SLN[RNS]NERL)	CASSLNRNERLFF	TRBV15	TRBJ1-4
					CASSLNNNERLFF	TRBV15	TRBJ1-4
					CASSLNNNERLFF	TRBV15	TRBJ1-4
					CASSLNSNERLFF	TRBV15	TRBJ1-4
			CASSRDRGNERLFF	([KS]RDRGNERL)	CASSRDRGNERLFF	TRBV13-3	TRBJ1-4
					CASSRDRGNERLFF	TRBV13-3	TRBJ1-4
					CASKRDRGNERLFF	TRBV13-3	TRBJ1-4
		Spleen	CASSLNNNERLFF	(SLNNNERL)	CASSLNNNERLFF	TRBV15	TRBJ1-4
					CASSLNNNERLFF	TRBV15	TRBJ1-4
					CASSLNNNERLFF	TRBV15	TRBJ1-4
			CAWRDWGSQNTLYF	([RK][DH]WGSQNTL)	CAWRDWGSQNTLYF	TRBV31	TRBJ2-4
					CAWRDWGSQNTLYF	TRBV31	TRBJ2-4
					CAWKHWGSQNTLYF	TRBV31	TRBJ2-4
Control	Infected	Lung	CASSQDWGGYAEQFF	(SQDWGGYAEQ)	CASSQDWGGYAEQFF	TRBV5	TRBJ2-1
					CASSQDWGGYAEQFF	TRBV5	TRBJ2-1
					CASSQDWGGYAEQFF	TRBV5	TRBJ2-1
PNG:RBD	Infected	Lung	CASSLNNNERLFF	(SLN[RN]NERL)	CASSLNNNERLFF	TRBV15	TRBJ1-4
					CASSLNNNERLFF	TRBV15	TRBJ1-4
					CASSLNRNERLFF	TRBV15	TRBJ1-4
					CASSLNNNERLFF	TRBV15	TRBJ1-4
			CASSDWGNQDTQYF	(SDWG[ND]QDTQ)	CASSDWGNQDTQYF	TRBV13-3	TRBJ2-5
					CASSDWGDQDTQYF	TRBV13-3	TRBJ2-5
					CASSDWGNQDTQYF	TRBV13-3	TRBJ2-5
					CASSDWGNQDTQYF	TRBV13-3	TRBJ2-5
			CASSPRQGGNTEVFF	(S[LP]RQG[AG][ND]TEV)	CASSLRQGGNTEVFF	TRBV5	TRBJ1-1
					CASSPRQGADTEVFF	TRBV5	TRBJ1-1
					CASSPRQGGNTEVFF	TRBV5	TRBJ1-1
			CASSLRQGGNTEVFF	(S[LP]RQG[AG]NTEV)	CASSLRQGGNTEVFF	TRBV5	TRBJ1-1
					CASSLRQGANTEVFF	TRBV5	TRBJ1-1
					CASSPRQGGNTEVFF	TRBV5	TRBJ1-1
			CASSLLGGRDTQYF	(SLLGGRDTQ)	CASSLLGGRDTQYF	TRBV16	TRBJ2-5
					CASSLLGGRDTQYF	TRBV16	TRBJ2-5
					CASSLLGGRDTQYF	TRBV16	TRBJ2-5
			CASSPDRIAEVFF	(S[RP]DR[GIV]?[AG]E[QV])	CASSPDRGEVFF	TRBV14	TRBJ1-1
					CASSPDRVAEQFF	TRBV14	TRBJ2-1
					CASSPDRIAEVFF	TRBV14	TRBJ1-1
					CASSRDRGAEVFF	TRBV14	TRBJ1-1
			CAWNHNYAEQFF	([ND][HFS]NYAEQ)	CAWNHNYAEQFF	TRBV31	TRBJ2-1
					CACDSNYAEQFF	TRBV31	TRBJ2-1
					CAWDFNYAEQFF	TRBV31	TRBJ2-1
		Spleen	CASSLNNNERLFF	(SLN[NG]NERL)	CASSLNNNERLFF	TRBV15	TRBJ1-4
					CASSLNNNERLFF	TRBV15	TRBJ1-4
					CASSLNGNERLFF	TRBV15	TRBJ1-4
					CASSLNNNERLFF	TRBV15	TRBJ1-4
			CASSQDWGQDTQYF	(SQDWGQDTQ)	CASSQDWGQDTQYF	TRBV5	TRBJ2-5
					CASSQDWGQDTQYF	TRBV5	TRBJ2-5
					CASSQDWGQDTQYF	TRBV5	TRBJ2-5
			CASSPSSYEQYF	(SPSSYEQ)	CASSPSSYEQYF	TRBV3	TRBJ2-7
					CASSPSSYEQYF	TRBV3	TRBJ2-7
					CASSPSSYEQYF	TRBV3	TRBJ2-7
			CGARDWGSSYEQYF	(RDWGSSYEQ)	CGARDWGSSYEQYF	TRBV20	TRBJ2-7

Table 1 (continued) | List of identified meta-clonotypes

Treatment	Virus	Organ	Centroids cdr3_b_aa	CDR3 motif	Enriched clonotypes	v_b_gene	j_b_gene
					CGARDWGSSYEQYF	TRBV20	TRBJ2-7
					CGARDWGSSYEQYF	TRBV20	TRBJ2-7
Naked RBD	-	Lung	CASSLGQYTEVFF	(S[LS]GQ[HY]TEV)	CASSLGQYTEVFF	TRBV12-1	TRBJ1-1
					CASSLGQGYTEVFF	TRBV12-1	TRBJ1-1
					CASSLGQYTEVFF	TRBV12-1	TRBJ1-1
					CASSSGQHTEVFF	TRBV12-1	TRBJ1-1
			CTCSAGTGGAPDTQYF	(SA[G]TGG[A][QP]DTQ)	CTCSATFFAQDTQYF	TRBV1	TRBJ2-5
					CTCSAGTGGAPDTQYF	TRBV1	TRBJ2-5
					CTCSAGTGGQDTQYF	TRBV1	TRBJ2-5
			CASSPSSYEQYF	(SPSSYEQ)	CASSPSSYEQYF	TRBV3	TRBJ2-7
					CASSPSSYEQYF	TRBV3	TRBJ2-7
					CASSPSSYEQYF	TRBV3	TRBJ2-7

among the four groups. Virus infection significantly increased the meta-clonotype number in the PNG:RBD vaccinated mice, indicating that virus infection promoted the expansion of antigen-specific T cells induced by the PNG:RBD vaccine (Fig. 6g). These findings show that an increase in TCR diversity after viral infection in the vaccinated mice is led by an increase in the frequency of various vaccine-induced antigen-specific $CD8^+$ T cells. The induction of various antigen-specific T cells at a low frequency by vaccination before virus infection likely contributed to the increase in TCR diversity after viral infection. We confirmed that antigen-specific T cells induced by the PNG:RBD vaccine included various antigen-specific T cell clones with one copy (Supplementary Fig. 15a). Moreover, a decrease in the number of low frequent T clone or diversity index score was observed after blocking SIGN-R1. However, SIGN-R1 blocking does not influence the frequency of the top 10 clones (Supplementary Fig. 15). These results suggest that antigen presentation through SIGN-R1 may contribute to induction of TCR with low frequency but high expansion ability. Finally, we conducted a gene expression profiling analysis of antigen-specific T cells induced by the PNG vaccine using scRNA-seq to reveal the characteristics of low-frequency antigen-specific T cells. The antigen-specific $CD8^+$ T cells were classified into seven clusters based on their gene expression profiles (Fig. 7a). The T cells in cluster 1 exhibited high expression of Cxcr3 and Gpr183; cluster 2 T cells showed elevated expression of Gzmk and Klre; cluster 3 T cells had high expression of Cd5 and Cd6, and cluster 5 T cells were characterized by high expression of Ccr7 and Sell. Additionally, although Il7r was highly expressed in cluster 5, it was also found to be expressed in other clusters (Fig. 7b, c). In contrast, Ifng was expressed in other clusters but not in cluster 5. No expression of Il2 was observed in any of the clusters, while Prf1 was expressed in all clusters (Fig. 7b, c). Next, antigen-specific T cell clones were divided into three groups according to their detection frequency, and the antigen-specific T cells in each group were characterized. Clones with a detection frequency of 2% or higher, between 0.05% and less than 2%, and lower than 0.05% were defined as high-, medium-, and low-frequency T cell clones, respectively. Most of the T cell clones with a medium or high frequency were observed in clusters 0 and 1, whereas low-frequency T cell clones were observed in those clusters, plus many in cluster 5 (Fig. 7d, e). Further analysis of expressed genes revealed that Gzma, Gzmk, and Cxcr3 were highly expressed in clones with a medium or high detection frequency, whereas Ccr7 and Sell were highly expressed in clones with a low detection frequency (Fig. 7f, g). In addition, Rgs10, involved in T cell adhesion; Rflnb, a known component of the TGF-beta pathway; and Pecam1, which is highly expressed in naïve or memory T cells in peripheral blood before TCR stimulation, were also highly expressed in low-frequency T cells (Fig. 7f, g). Considered together, these results suggest that low-frequency T cells induced by the PNG vaccine exhibit naïve or memory-like phenotypes with weak effector functions and might expand vigorously after SARS-CoV-2 infection.

Discussion

Using PNG, a lymph node macrophage-selective delivery system, we successfully developed a novel protein vaccine that strongly induces antigen-specific $CD8^+$ T cells and antibodies. This study is the first to demonstrate that PNG binds to the CRD domain of SIGN-R1 on mouse medullary macrophages and efficiently delivers antigens to these cells. We previously showed that medullary macrophages can strongly activate vaccine-specific $CD8^+$ T cells in the presence of TLR stimulation. Several studies showed that antigen delivered through specific C-type lectin receptor, such as DEC-205 or mannose receptor[51–54], to antigen-presenting cells is efficiently presented to $CD8^+$ T cells as cross-presentation, therefore it is possible that vaccine antigens incorporated by medullary macrophages through SIGN-R1 may also be presented to T cells efficiently via a similar mechanism. Indeed, it was previously demonstrated that DC-SIGN, a human counterpart of murine SIGN-R1, efficiently internalize bound antigen and present it to T cells[55]. These findings support the efficacy of the SIGN-R1-targeting by the PNG vaccine delivery system to induce a strong $CD8^+$ T cell response, which is considered the key underlying mechanism for virus clearance. In humans, DC-SIGN (CD209) is also highly expressed in lymph node medullary macrophages[56]. Therefore, the PNG-based vaccine shows great potential for translation into human subjects. However, the roles and functions of human lymph node medullary macrophages are still elusive, and require further research. We also demonstrated that virus clearance by the PNG:RBD vaccine is dependent on both $CD8^+$ T cells and antibodies. Previous studies have suggested that $CD8^+$ T cells are not associated with vaccine-induced viral clearance, whereas others suggested that virus-specific $CD8^+$ T cells contribute to viral clearance. In natural infections, $CD8^+$ T cells have been demonstrated to contribute significantly to viral clearance when antiviral antibodies have a low contribution[32]. We employed the RBD fragment of the S protein of SARS-CoV-2 as the vaccine antigen in this study. In general, the binding of vaccine-induced antibodies to the S protein is relatively weak when a partial fragment of the S protein is used, since the conformation of the fragment is different from that of the full-length S protein. Although we confirmed the clear inhibition of binding between RBD and hACE2 by vaccine-induced serum antibodies, the affinity of these antibodies might be relatively low and may lead to the observed contribution of vaccine-induced $CD8^+$ T cells in virus clearance. Therefore, our findings are especially meaningful in the contexts where neutralizing antibodies are not effective. For example, for variants of concern (VOCs), such as the Omicron strain, that evade antibodies induced by conventional vaccines, vaccines that strongly induce cellular immunity, including our pullulan PNG-based vaccine, could be effective.

$CD8^+$ T cell-dependent elimination of viral infection is accompanied by the accumulation of neutrophils in the lungs, inducing

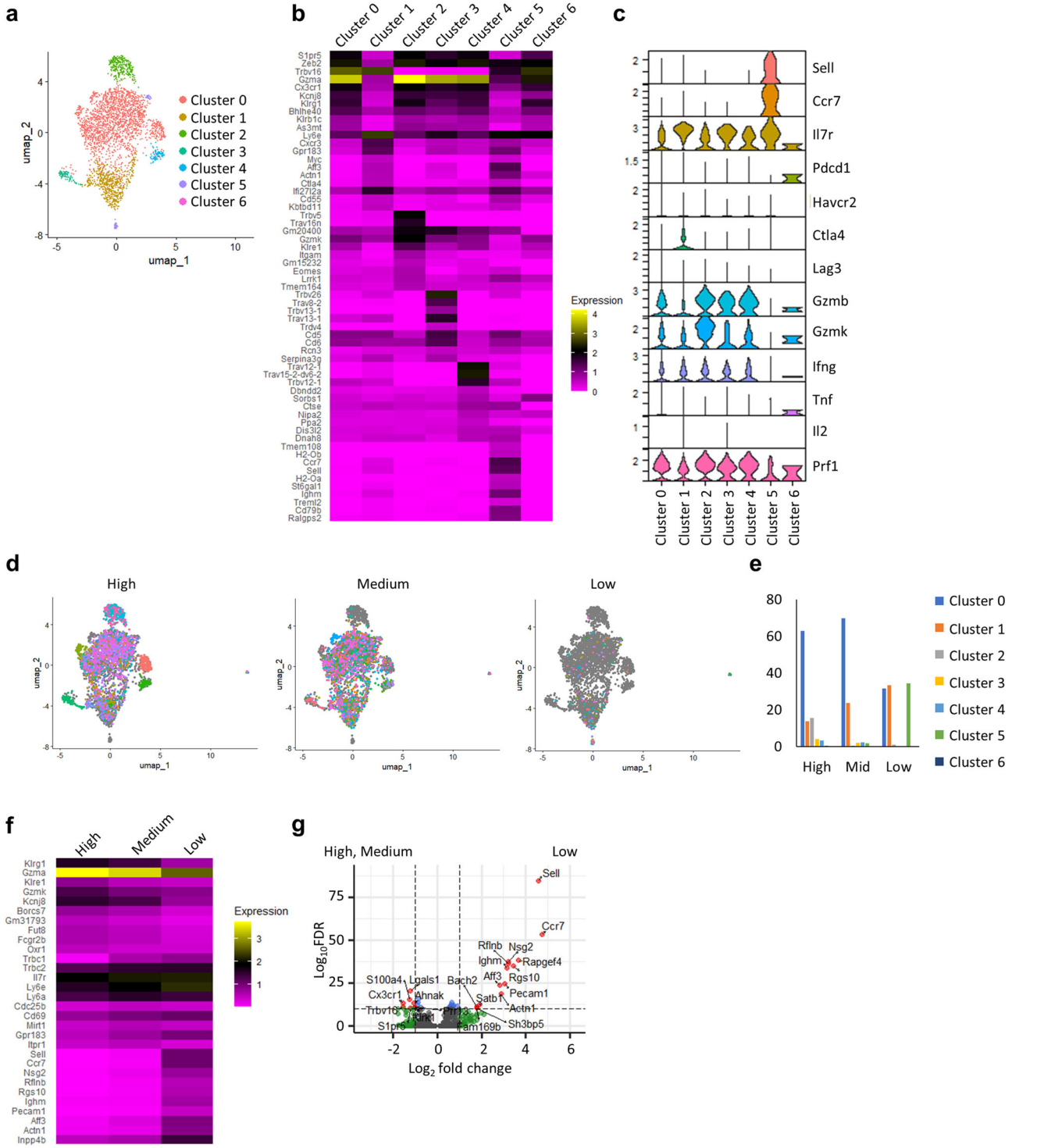

Fig. 7 | Characteristics of antigen-specific low-frequency T cells. K18-hACE2 mice were immunized twice with the PNG:RBD vaccine at a 2-week interval. Splenocytes were collected 21 days after the second vaccination, and scRNA-seq was performed (pooled from three mice). **a** Uniform Manifold Approximation and Projection (UMAP) of the expression profiles of antigen-specific T cells induced by PNG:RBD vaccine. $CD8^+$ T cells are classified into seven distinct transcriptional clusters. **b** Relative expression of the top ten most differentially expressed genes in each cluster. **c** Violin plots quantifying the relative transcriptional expression of genes of memory naïve markers, exhausted markers, and cytokines. **d**, **e** UMAPs of T cells in each frequency group. **f** Relative expression of the top ten most differentially expressed genes in each frequency group. **g** Analysis of genes differentially expressed between mid- and high-frequency and low-frequency antigen-specific T cells.

intense inflammation[57]. However, in this study, such strong inflammatory responses or changes in inflammation-related gene expression were not observed in the vaccinated mice, as determined by RNA-seq. Additionally, there were no significant differences in the gene expression signatures between the vaccinated and control mice, as determined by CIBERSORT. This may be due to a rapid clearance of the virus by vaccine-induced immune responses prior to the establishment of SARS-CoV-2 infection.

In this study, vaccination with the PNG:RBD vaccine significantly increased TCR clonality in the lungs and spleens, which corresponded to a

strong correlation of TCR repertoires between these organs (Fig. 6c, d). In the vaccinated group, TCR clonality was increased by vaccination but decreased after virus infection. In addition, the correlation of TCR repertoires between the lungs and spleens was low compared with that in the vaccinated mice prior to virus challenge. As SARS-CoV-2 infects host respiratory cells after exposure through inhalation and spreads systemically thereafter, the immune responses against the virus in each organ may develop independently at first[58], which is consistent with our finding of unique TCR profiles between the lung and spleen.

We performed meta-clonotype analysis of the TCR repertoire to explore the changes in TCRs in more detail. Meta-clonotype analysis is a method to group TCRs based on the CDR3 sequence and biochemical characteristics. The CDR3 sequence in TCR is highly associated with the antigen recognized by TCR, and TCRs with similar CDR3 sequences are considered to recognize the same antigen. A previous study reported that meta-clonotypes targeting specific antigens were detected in more than 59.7% of COVID-19 patients[59]. In the vaccinated mice in this study, virus infection increased TCR diversity and detectable meta-clonotypes, suggesting that virus infection expanded the antigen-specific $CD8^+$ T cell clones. It is possible that antigen-specific TCRs that were first infrequent post-vaccination expanded with viral infection and became detectable. Meta-clonotypes detected after viral infection were also detected at a low frequency before viral challenge in the vaccinated mice, showing that these meta-clonotype T cells were already induced by the vaccine, although at a very low rate. Considering that TCR diversity is correlated with the efficacy of preventive vaccination after virus infection[60,61] and that the rate of meta-clonotypes detected at high frequency after vaccination was significantly reduced after viral infection, we hypothesized that virus-specific T cells induced by the vaccine at high frequency might not necessarily contribute to the elimination of the virus, and that the low-frequency vaccine-elicited T cells might contribute more to the clearance of SARS-CoV-2 in the lung after vaccination.

Several studies have described antigen-specific T cells with high proliferative abilities. The BioNTech mRNA vaccine can induce vaccine-specific stem cell memory T cells with a high proliferative ability, while the PNG:RBD vaccine induces vaccine-specific $CD8^+$ T cells, including various clones showing naïve or memory-like phenotype. These findings suggest that a large number of poor-quality antigen-specific $CD8^+$ T cells in vaccinated patients may not confer the protection against viral infection, or the protection against viral infection may be achieved even if antigen-specific T cells are not detected after vaccination if these T cells are highly reactive to restimulation. In antibody-dependent defense against infection, the number of antigen-specific antibodies, which block the binding of the receptor to the virus, is important in controlling viral infection. However, in the protection against viral infection by cellular immune responses, the quality of antigen-specific T cells may be more important than their numbers.

It is believed that in the defense against viral infection at local sites by cellular immune responses with prophylactic vaccines, virus-specific vaccine-induced T cells proliferate explosively and eliminate virus-infected cells after recognizing viral antigens; however, it is unclear how vaccine-induced T cells eliminate the virus after infection in the lungs, for example. Since the TCR repertoires differ greatly among individual mice, it is difficult to analyze changes over time, for example, by comparing the repertoire before and after vaccination. In this study, we overcame this limitation and were able to detect the changes in the TCR repertoires in the lungs using meta-clonotype analysis.

Current vaccines depending on $CD8^+$ T cells exert their protective effects when vaccine-specific T cells are activated by viral infection in vivo, but our study suggests that a comprehensive activation of T cells with various properties to the virus-specific antigen (same antigen) can lead to the efficient removal of virus-infected cells and, ultimately, virus elimination. Future studies should consider developing a vaccine that more efficiently eliminates SARS-CoV-2 by inducing a higher diversity of antigen-specific $CD8^+$ T cells.

Methods

Mice

B6.Cg-Tg(K18-ACE2)2Prlmn/J mice (K18-hACE2), C57BL/6JJcl, and BALB/c mice were purchased from Jackson Laboratory or Japan SLC respectively. DUC18 mice, transgenic for TCRα/β-reactive with a Kd-restricted 9 m epitope, were established as previously described[62]. The mice were maintained at the Animal Center of Nagasaki University Graduate School of Medicine (Nagasaki, Japan) and were used at 7–11 weeks of age. The experimental protocol was approved by the Ethics Review Committee for Animal Experimentation of Nagasaki University Graduate School of Medicine (Approval no. 201007-1). SARS-CoV-2 infection experiments were conducted in a BSL-3 facility in accordance with local regulations and biosafety guidelines.

Cell lines and virus propagation

HeLa cells were cultured in DMEM containing 10% fetal bovine serum (FBS, NICHIREI) and antibiotics at 37 °C in 5% CO_2. Vero 9013 cells (Japan Health Science Research Resources Bank) were cultured as previously described in Eagle's Minimum Essential Medium (EMEM, Sigma-Aldrich, St. Louis, MO, USA) supplemented with 10% fetal calf serum (FCS, Gibco) without antibiotics at 37 °C in 5% CO_2. SARS-CoV-2 (TY-WK-521/2020 strain) was propagated in Vero 9013 cells at 37 °C and 5% CO_2 for up to 6 days.

Immunization of mice

The PNG:RBD vaccine (20 μg protein) or 20 μg of RBD alone protein or was mixed with 25 μg K3 CpG oligoDNA in 100 μL PBS and then subcutaneously injected into the right flank of mice at a 2-week interval after anesthetization with inhalation of 3–5% isoflurane. For the depletion of $CD8^+$ T and B cells, anti-CD8 and anti-CD20 antibodies (100 μg/mouse), respectively, were intravenously injected into the mice. The PNG-long peptide antigen complex was subcutaneously injected into the back of BALB/c mice at a dose of 20 μg peptide.

Virus challenge in mice

K18-hACE2 transgenic mice were lightly sedated with inhalation isoflurane and intranasally infected with SARS-CoV-2 virus at a dose of 5×10^4 PFU/mouse. Non-infected control mice were inoculated with vehicle medium. The infected mice were euthanized, and saliva and selected tissues were collected for further analysis.

Antibodies and reagents

Phycoerythrin (PE)-conjugated anti-CD8 monoclonal antibody (mAb, 53-6.7, rat IgG2a), Brilliant Violet 421-conjugated anti-CD197 mAb (4B12, rat IgG2a), Brilliant Violet 711-conjugated anti-mouse CD127 mAb (A7R34, rat IgG2a), PE/Cyanine7-conjugated anti-mouse/human CD45R/B220 mAb (RA3-6B2, rat IgG2a), allophycocyanin (APC)/Cyanine7-conjugated anti-mouse/human CD44 mAb (IM7, rat IgG2b), APC-conjugated anti-mouse CD206 mAb (C068C2, rat IgG2a), Brilliant Violet 510-conjugated anti-mouse/human CD11b mAb (M1/70, rat IgG2b), APC/Cyanine7-conjugated anti-mouse CD11c mAb (N418, Armenian Hamster IgG), PerCP/Cyanine5.5-conjugated anti-mouse CD169 mAb (3D6.112, rat IgG2a), APC-conjugated anti- mouse/human KLRG1 (MAFA) mAb (2F1/KLRG1, Syrian Hamster IgG), PE-conjugated anti-mouse NKG2A mAb (16A11, mouse IgG2b), PerCP/Cyanine5.5-conjugated anti-mouse CD3 mAb (17A2, rat IgG2b), PE/Cy7-conjugated anti-mouse CD49b mAb (DX5, rat IgM), Brilliant Violet 421-conjugated anti-mouse CD25 mAb (PC61, rat IgG1), FITC-conjugated anti-mouse CD4 mAb (GK1.5, rat IgG2b), PerCP/Cyanine5.5-conjugated anti-mouse CD27 mAb (LG.3A10, Armenian hamster IgG), PE-conjugated anti-mouse CD137 mAb (1AH2, rat IgG1), PE/Cy7-conjugated anti-mouse GITR mAb (DTA1, rat IgG2b), Brilliant Violet 650-conjugated anti-mouse CD69 mAb (H1.2F3, Armenian hamster IgG) were purchased from BioLegend (San Diego, CA, USA). FITC-conjugated anti-CD8 mAb (KT15, rat IgG2a), anti-mouse Mincle mAb (4A9, rat IgG1), Peroxidase-conjugated anti-mouse IgG (H + L chain), anti-mouse IgG1 (H + L chain), and anti-mouse IgG2 (H + L

chain) were purchased from MBL (San Diego, CA, USA). For tetramer staining, S_{539}-specific tetramers were generated as per the manufacturer's instructions (QuickSwitch™ Quant H-2Kb tetramer kit, MBL) with RBD peptide (S_{539}, 10 μM). APC-conjugated anti-interferon-gamma (XMG1.2, rat IgG1) was purchased from eBioscience (San Diego, CA, USA). APC-conjugated anti-mouse CD209a (5H10, rat IgG2a), PE-conjugated anti-mouse CD137 mAb (1AH2, rat IgG1), and PE/Cy7-conjugated anti-mouse GITR mAb (DTA1, rat IgG2b) was purchased from BD Biosciences (Oxford, UK). FITC-conjugated anti-mouse Dectin1 (2A11, rat IgG2b) was purchased from Bio-Rad Laboratories (Hercules, CA, USA). FITC-conjugated anti-Rat IgG (H + L) Secondary Antibody (2A11, rat IgG2b) was purchased from Thermo Fisher Scientific. Depleting antibodies, including anti-CD8α (clone 53-6.7) and anti-CD20 (clone MB20-11), and the blocking antibody anti-CD209b (clone 22D1) were purchased from Bio X Cell (Lebanon, NH, USA). RBD peptides (S_{395}, S_{511}, and S_{539}) were obtained from GenScript (Tokyo, Japan). A phosphorothioate oligodeoxynucleotide containing an unmethylated CpG motif (K3 CpG ODN, 5′-ATCGACTCTCGAGCGTTCTC-3′) was synthesized by Gene Design (Osaka, Japan). The C-type lectin complementary DNA (cDNA) plasmids were purchased from Genecopoeia (Rockville, MD, USA).

Uptake of PNG in mouse C-type lectin-expressing cells

Each C-type lectin cDNA plasmid was introduced into HeLa cells by electroporation and seeded onto a 24-well plate. The next day, the cells were incubated with 2 μg/mL rhodamine-labeled PNG at 37 °C for 30 min. Anti-CD209b antibody (22D1) was added to the wells 1 h before the addition of rhodamine-labeled PNG for blocking. The rhodamine signal was measured by flow cytometry (BD LSR Fortessa X-20) or microscopy (Keyence). The data were analyzed using FlowJo software (TOMY Digital Biology, Tokyo, Japan).

Tracking of subcutaneously injected PNG

Rhodamine-labeled PNG was subcutaneously injected into the right flank of the mice. Immune cells were collected from the inguinal DLN 10 min after injection and analyzed by flow cytometry (BD LSR Fortessa X-20) to measure the rhodamine signal in lymph node macrophages. The data were analyzed using FlowJo software. Cryosections of the inguinal DLN were prepared for immunohistochemistry. OCT-embedded sections were stained with a fluorescent dye-conjugated anti-CD209b antibody and observed under a fluorescence microscope. Anti-CD209b antibody was subcutaneously injected into mice 1 h before the administration of rhodamine-PNG for blocking.

Ex vivo antigen presentation

Antigen presentation by macrophages was evaluated ex vivo by measuring antigen-specific proliferation of $CD8^+$ T cells as previous report[39]. Briefly, PNG-mutated ERK2 long peptide antigen (NDHIAYFLYQILRGLQYIHSA NVLHRDLKPSNLLLNT) complex and CpG ODN were subcutaneously injected into BALB/c mice. Anti-CD209b antibody was subcutaneously injected into mice 1 h before the administration of PNG-antigen for blocking. The lymph node was resected 18 h after injection and macrophages were purified with anti-CD11b microbeads (Miltenyi Biotec). Isolated cells were cocultured with 1.0×10^5 DUC18 T cells prelabeled with a Farred dye for 72 h. T cell proliferation was determined by quantifying dye dilution on a flow cytometry (BD LSR Fortessa X-20). The data were analyzed using FlowJo software (TOMY Digital Biology, Tokyo, Japan).

PNG:RBD vaccine

We produced a recombinant RBD fragment of the SARS-CoV-2 S protein (319–546 aa) fused to a leader sequence and a histidine tag at the N and C terminus, respectively. The protein was expressed in CHO-K1 cells and purified using Ni-NTA affinity and gel filtration chromatography. Protein purity was confirmed by SDS-PAGE and SE-HPLC. Cholesteryl pullulan was purchased from NOF Co. Ltd. (Tokyo, Japan). A solution of cholesteryl pullulan phosphate-buffered saline (PBS) containing 6 M urea was combined with a solution of RBD protein. The mixture was gently stirred at 4 °C overnight and subjected to dialysis against PBS to remove urea. During this step, the protein was incorporated into the PNG formed by the self-assembly of cholesteryl pullulan. Formation of the complex between the protein and PNG was confirmed by SE-HPLC. The obtained solution was stored at 4 °C until use.

Intracellular cytokine and tetramer staining

For intracellular cytokine staining, vaccinated or infected mice were anesthetized under isoflurane inhalation (3–5%), and splenocytes were collected. The splenocytes were then incubated with a synthetic RBD-derived $CD8^+$ T cell epitope peptide for 30 min at 37 °C, incubated for an additional 16 h with GolgiPlug (BD Biosciences), and stained with a PE-conjugated anti-CD8 mAb. Permeabilization and fixation were performed using a Cytofix/Cytoperm kit (BD Biosciences) according to the manufacturer's instructions. The cells were stained intracellularly with an APC-conjugated anti-IFN-γ antibody and analyzed on a flow cytometer (FACS Canto II) after being washed. The data were analyzed using FlowJo software. Tetramer staining was performed as previously described[63]. Briefly, cells were stained with PE-labeled S395/Kb tetramer for 15 min at room temperature and then stained with antibodies for surface markers for 15 min at 4 °C. After washing, the cells were analyzed using flow cytometry.

RBD antibody ELISA

RBD protein-specific antibody responses were assessed using ELISA. Briefly, the recombinant RBD protein was absorbed onto a immunoplates (Nunc, Roskilde, Denmark) at a concentration of 10 ng/50 μL/well at 4 °C. The serum collected from the immunized mice was diluted from 1:300 to 1:8,100. After washing and blocking the plate, diluted sera were added and incubated for 10 h. After washing, peroxidase-conjugated anti-mouse IgG (H + L chain), anti-mouse IgG1 (H + L chain), or anti-mouse IgG2 (H + L chain; MBL, Nagoya, Japan) was added. After adding TMB substrate (Pierce, Rockford, IL, USA), the plate was analyzed using a microplate reader (Model 550, Bio-Rad Laboratories).

Neutralization activity

Virus titration was performed using a conventional plaque assay. The cells were seeded in 12-well plates with 1 mL EMEM supplemented with 10% FBS and incubated at 37 °C in 5% CO_2 overnight to allow the formation of a monolayer. Mouse plasma samples were serially diluted two-fold in EMEM from 1:10 to 1:1,280. A total of 50 μL of virus mixture (100 PFU per well) was added to equal amounts of diluted plasma. The virus and antibody mixture was incubated at 37 °C for 60 min, and 100 μL of serially diluted sample was added to each well. At least two replicates were performed for each sample. The plates were incubated at 37 °C in 5% CO_2 for 60 min, with plate tilting every 10 min. After incubation, 1 mL of overlay medium was added to each well. After 4 days of incubation, the cells were fixed with 4% paraformaldehyde for 1 h at room temperature and stained with 0.25% crystal violet (Wako Pure Chemical Industries, Osaka, Japan). After washing and drying the plates, the number of plaques was counted with the naked eye. Neutralization was defined as a 50% or higher plaque reduction compared to that in the control (infection in the absence of plasma).

Viral RNA quantitation

Viral RNA was extracted from 100 μL of liquid samples using a Quick Viral RNA kit (Zymo Research, Tustin, CA, USA), and the SARS-CoV-2 E gene was amplified using quantitative RT-PCR[64]. Used primers are shown in Table 2. Viral RNA was subjected to quantitative RT-PCR as previously described[65].

RNA-seq

RNA was extracted from organs collected 3 days post infection, and RNA quality was assessed using spectrophotometry and an Agilent Bioanalyzer 2100 (Agilent Technologies). The total RNA library was prepared using a SMART-Seq® HT Kit (Takara Bio USA, Mountain View, CA, USA) and Nextera XT DNA Library Prep Kit (Illumina, San Diego, CA, USA). An Illumina NovaSeq 6000 system (Illumina) was used to sequence the libraries for 2 × 150 cycles. RNA-seq data are available in the DNA Data Bank of Japan (DDBJ) under accession numbers DRA016618.

Table 2 | Primers used in this study

Identification	Sequence
BSL-18E	AAAGCGGCCGCATGCTTTTTTTTTTTTTTTTTTVN
P20EA	TAATACGACTCCGAATTCCC
P10EA	GGGAATTCGG
P22EA-ST1-R	GTCTCGTGGGCTCGGAGATGTGTATAAGAGACAGC TAATACGACTCCGAATTCCC
mCB1	AGGATTGTGCCAGAAGGTAG
mCB2	TTGTAGGCCTGAGGGTCC
mCB-ST1-R	TCGTCGGCAGCGTCAGATGTGTATAAGAGACAGGTT GGGTGGAGTCACATTT
N_Sarbeco_F1	CACATTGGCACCCGCAATC
N_Sarbeco_R1	GAGGAACGAGAAGAGGCTTG
N_Sarbeco_P1-FAM	ACTTCCTCAAGGAACAACATTGCCA-BBQ

Unbiased amplification of TCR genes with AL-PCR

Total RNA was converted to cDNA using Superscript III reverse transcriptase (Invitrogen). TCR genes were amplified by adaptor ligation-mediated PCR[66,67]. Used primers are shown in Table 2. High-throughput sequencing was performed using an Illumina MiSeq paired-end platform (2 × 300 bp, Illumina). TCR sequence data are available in the DDBJ under accession numbers DRA016643.

Assignment of TRAV, TRAJ, TRBV, and TRBJ segments

Assignment of TRAV, TRAJ, TRBV, and TRBJ segments in TCR genes was performed based on the international ImMunoGeneTics information system® database (http://www.imgt.org). Data processing, assignment, and aggregation were automatically performed using repertoire analysis software originally developed by Repertoire Genesis (Osaka, Japan).

Analysis of TCR data

A unique sequence read (USR) was defined as one having no identity in TRBV, TRBJ, and deduced amino acid sequence of CDR3 with the other sequence reads. The copy numbers of identical USRs were automatically counted using Repertoire Genesis software for each sample and then ranked in order of copy number. We then calculated the percentage occurrence frequencies of sequence reads with TRBV and TRBJ genes from the total sequence reads.

Immune infiltration analysis based on cell type identification by CIBERSORTx

CIBERSORTx (https://cibersort.stanford.edu/) was used to analyze the immune landscape of the lung and spleen with RNA-seq data used as the gene expression input and 511 mouse gene expression (25 immune cell types)[68] set as the signature gene file. The generated CIBERSORTx values were defined as the immune cell infiltration fraction per sample.

Identification of expanded meta-clonotypes

We used tcrdist3 (v0.2.2), which implements the TCR distance metric, to search for candidate antigen-associated TCRs that are likely to confer immunity against SARS-CoV-2. Based on the idea that the same or similar clonotypes tend to appear in multiple samples from a similar antigen-stimulated population, this framework defines a "meta-clonotype" as a set of similar TCR clonotypes shared by multiple samples from a target population compared to a control background. In short, it enables efficient identification of the sequence space in which TCRs sharing a high degree of sequence similarity in terms of biochemical features and motifs of CDR3 are enriched among a target population. As a data preprocessing step for meta-clonotype identification, we selected clonotypes with at least 32 reads detected in each sample in the same group to reduce computational cost and focus on clonally expanded T cells. Following the documentation of tcrdist3, we set the background repertoire to 200,000 synthetic TCRs with a matching V-J gene and 100,000 randomly subsampled TCRs from samples of the control group as an antigen-naïve population. In searching meta-clonotypes, tcrdist3 computes a TCRdist distance matrix between all given clonotypes. The centroids of the meta-clonotype are identified by the enrichment of neighbor clonotypes from multiple samples in the target population compared to the background within the optimized radii. The optimized radius was defined for each clonotype by the relative density of adjacent TCRs in the background. In our case, the largest radius was set within a reasonable scope that contained less than an estimated proportion of $1E-5$ TCRs in the background, along with an upper radius limit (24 TCRdist units). Furthermore, we added a constraint that meta-clonotypes are formed from clonotypes from all samples in the same group.

Preparation of single-cell complementary DNA libraries

Splenocytes isolated from the vaccinated mice were stained with PE-labeled S395/Kb tetramer for 15 min at room temperature and then stained with antibodies for surface markers for 15 min at 4 °C. Zombie NIR Fixable Viability Kit (BioLegend) was used to exclude dead cells. RBD-specific $CD8^+$ T cells were sorted on an Aria III (BD Biosciences). Single-cell suspensions were subjected to GEM (Gel Bead-In Emulsions) generation and barcoding using the Chromium Next GEM Single Cell 5′ GEM Kit V.2 (PN-1000244) on the Chromium Next GEM Chip K Single Cell Kit (PN-1000286), according to the manufacturer's instructions (10x Genomics, Pleasanton, California, USA). Collected complementary DNAs (cDNAs) from GEMs were amplified, and TCR target amplification was performed using a TCR Amplification Kit (PN-1000254). The TCR and gene expression cDNA libraries were constructed using the Library Construction Kit (PN-1000190). The cDNA was sequenced using a NovaSeq System (Illumina, San Diego, California, USA) with a pair-end 150 bp sequencing strategy.

Preprocessing of paired scRNA-seq and scTCR-seq data

Raw sequencing data for RNA expression and VDJ from mouse $CD8^+$ T scRNA-seq were processed using Cell Ranger software (V.6.0.1; 10x Genomics). RNA expression data were aligned to the mm10 reference genome and VDJ sequencing data to the GRCm38 VDJ reference pre-built by 10x Genomics. Gene expression count matrices were imported into the R package Seurat (V.4.1.0) using R (V.4.1.3). Cells were filtered to retain those with ≤10% mitochondrial RNA content and several unique molecular identifiers numbered between 200 and 5000. RNA expression data were normalized against total expression per cell and natural log transformed with a scale factor of 10,000. Counts were log-normalized, scaled, and centered. The 2000 most-variable features were calculated with variance-stabilizing transformation and used for principal component analysis. Clustering was performed with Seurat: FindClusters, with the resolution set to 0.2. Dimension reduction was performed with Uniform Manifold Approximation and Projection. scRNA-seq and scTCR-seq data are available in the DDBJ under accession numbers DRA007761.

Statistical analysis

Data obtained in the virus challenge experiment were analyzed using the Steel–Dwass test. Data from the other experiments were analyzed using unpaired two-tailed Student's *t* tests and one-way or two-way analysis of variance (ANOVA) with a multiple comparisons Bonferroni post hoc test. Statistical significance was set at $p < 0.05$. FDR was calculated to compare RNA-seq data between multiple groups. A *p* value or FDR less than 0.05 was considered to indicate statistical significance. All error bars represent mean ± SD. The Kaplan–Meier method was used for survival analysis, using SPSS Advanced Statistics (v28, IBM SPSS, Armonk, NY, USA). All other statistical analyses were performed using R software (v4.2.2, The R Foundation for Statistical Computing, Vienna, Austria).

Data availability

Data supporting the findings of this study are available in this paper, Supplementary information, or are available from the corresponding authors, Daisuke Muraoka (d.muraoka@aichi-cc.jp) upon request. All sequence data are available from DDBJ (https://www.ddbj.nig.ac.jp/index.html).

Received: 3 July 2023; Accepted: 1 September 2024;
Published online: 18 September 2024

References

1. Zhu, N. et al. A novel coronavirus from patients with pneumonia in China, 2019. *N. Engl. J. Med.* **382**, 727–733 (2020).
2. Huang, C. et al. Clinical features of patients infected with 2019 novel coronavirus in Wuhan, China. *Lancet* **395**, 497–506 (2020).
3. Wu, F. et al. A new coronavirus associated with human respiratory disease in China. *Nature* **579**, 265–269 (2020).
4. Polack, F. P. et al. Safety and efficacy of the BNT162b2 mRNA Covid-19 vaccine. *N. Engl. J. Med.* **383**, 2603–2615 (2020).
5. Ramasamy, M. N. et al. Safety and immunogenicity of ChAdOx1 nCoV-19 vaccine administered in a prime-boost regimen in young and old adults (COV002): a single-blind, randomised, controlled, phase 2/3 trial. *Lancet* **396**, 1979–1993 (2021).
6. Sadoff, J. et al. Safety and efficacy of single-dose Ad26.COV2.S vaccine against Covid-19. *N. Engl. J. Med.* **384**, 2187–2201 (2021).
7. Voysey, M. et al. Safety and efficacy of the ChAdOx1 nCoV-19 vaccine (AZD1222) against SARS-CoV-2: an interim analysis of four randomised controlled trials in Brazil, South Africa, and the UK. *Lancet* **397**, 99–111 (2021).
8. Baden, L. R. et al. Efficacy and safety of the mRNA-1273 SARS-CoV-2 vaccine. *N. Engl. J. Med.* **384**, 403–416 (2021).
9. Lan, J. et al. Structure of the SARS-CoV-2 spike receptor-binding domain bound to the ACE2 receptor. *Nature* **581**, 215–220 (2020).
10. Barnes, C. O. et al. SARS-CoV-2 neutralizing antibody structures inform therapeutic strategies. *Nature* **588**, 682–687 (2020).
11. Khoury, D. S. et al. Neutralizing antibody levels are highly predictive of immune protection from symptomatic SARS-CoV-2 infection. *Nat. Med.* **27**, 1205–1211 (2021).
12. Yuan, M., Liu, H., Wu, N. C. & Wilson, I. A. Recognition of the SARS-CoV-2 receptor binding domain by neutralizing antibodies. *Biochem. Biophys. Res. Commun.* **538**, 192–203 (2021).
13. Zhou, D. et al. Evidence of escape of SARS-CoV-2 variant B.1.351 from natural and vaccine-induced sera. *Cell* **184**, 2348–2361 e2346 (2021).
14. Hoffmann, M. et al. SARS-CoV-2 variants B.1.351 and P.1 escape from neutralizing antibodies. *Cell* **184**, 2384–2393 e2312 (2021).
15. Wang, P. et al. Antibody resistance of SARS-CoV-2 variants B.1.351 and B.1.1.7. *Nature* **593**, 130–135 (2021).
16. Tegally, H. et al. Detection of a SARS-CoV-2 variant of concern in South Africa. *Nature* **592**, 438–443 (2021).
17. Washington, N. L. et al. Emergence and rapid transmission of SARS-CoV-2 B.1.1.7 in the United States. *Cell* **184**, 2587–2594 e2587 (2021).
18. Boehm, E. et al. Novel SARS-CoV-2 variants: the pandemics within the pandemic. *Clin. Microbiol. Infect.* **27**, 1109–1117 (2021).
19. Planas, D. et al. Reduced sensitivity of SARS-CoV-2 variant Delta to antibody neutralization. *Nature* **596**, 276–280 (2021).
20. Yadav, P. D. et al. Neutralization of variant under investigation B.1.617.1 with sera of BBV152 vaccinees. *Clin. Infect. Dis.* **74**, 366–368 (2022).
21. Akkiz, H. The biological functions and clinical significance of SARS-CoV-2 variants of corcern. *Front. Med.* **9**, 849217 (2022).
22. Edara, V. V. et al. Infection and vaccine-induced neutralizing-antibody responses to the SARS-CoV-2 B.1.617 variants. *N. Engl. J. Med.* **385**, 664–666 (2021).
23. Liu, J. et al. BNT162b2-elicited neutralization of B.1.617 and other SARS-CoV-2 variants. *Nature* **596**, 273–275 (2021).
24. Wall, E. C. et al. Neutralising antibody activity against SARS-CoV-2 VOCs B.1.617.2 and B.1.351 by BNT162b2 vaccination. *Lancet* **397**, 2331–2333 (2021).
25. Krause, P. R. et al. SARS-CoV-2 variants and vaccines. *N. Engl. J. Med.* **385**, 179–186 (2021).
26. Tregoning, J. S., Flight, K. E., Higham, S. L., Wang, Z. & Pierce, B. F. Progress of the COVID-19 vaccine effort: viruses, vaccines and variants versus efficacy, effectiveness and escape. *Nat. Rev. Immunol.* **21**, 626–636 (2021).
27. Long, Q. X. et al. Clinical and immunological assessment of asymptomatic SARS-CoV-2 infections. *Nat. Med.* **26**, 1200–1204 (2020).
28. Wu, F. et al. Evaluating the association of clinical characteristics with neutralizing antibody levels in patients who have recovered from mild COVID-19 in Shanghai, China. *JAMA Intern. Med.* **180**, 1356–1362 (2020).
29. Peng, Y. et al. Broad and strong memory CD4(+) and CD8(+) T cells induced by SARS-CoV-2 in UK convalescent individuals following COVID-19. *Nat. Immunol.* **21**, 1336–1345 (2020).
30. Rydyznski Moderbacher, C. et al. Antigen-specific adaptive immunity to SARS-CoV-2 in acute COVID-19 and associations with age and disease severity. *Cell* **183**, 996–1012 e1019 (2020).
31. Tan, A. T. et al. Early induction of functional SARS-CoV-2-specific T cells associates with rapid viral clearance and mild disease in COVID-19 patients. *Cell Rep.* **34**, 108728 (2021).
32. Kingstad-Bakke, B. et al. Vaccine-induced systemic and mucosal T cell immunity to SARS-CoV-2 viral variants. *Proc. Natl. Acad. Sci. USA* **119**, e2118312119 (2022).
33. Ishii, H. et al. Neutralizing-antibody-independent SARS-CoV-2 control correlated with intranasal-vaccine-induced CD8(+) T cell responses. *Cell Rep. Med.* **3**, 100520 (2022).
34. Hajnik, R. L. et al. Dual spike and nucleocapsid mRNA vaccination confer protection against SARS-CoV-2 Omicron and Delta variants in preclinical models. *Sci. Transl. Med.* **14**, eabq1945 (2022).
35. Dangi, T., Class, J., Palacio, N., Richner, J. M. & Penaloza MacMaster, P. Combining spike- and nucleocapsid-based vaccines improves distal control of SARS-CoV-2. *Cell Rep.* **36**, 109664 (2021).
36. Zoratto, N. et al. Strategies to load therapeutics into polysaccharide-based nanogels with a focus on microfluidics: a review. *Carbohydr. Polym.* **266**, 118119 (2021).
37. Ma, X. et al. Bioengineered nanogels for cancer immunotherapy. *Chem. Soc. Rev.* **51**, 5136–5174 (2022).
38. Gu, X. G. et al. A novel hydrophobized polysaccharide/oncoprotein complex vaccine induces in vitro and in vivo cellular and humoral immune responses against HER2-expressing murine sarcomas. *Cancer Res.* **58**, 3385–3390 (1998).
39. Muraoka, D. et al. Nanogel-based immunologically stealth vaccine targets macrophages in the medulla of lymph node and induces potent antitumor immunity. *ACS Nano* **8**, 9209–9218 (2014).
40. Muraoka, D., Harada, N., Shiku, H. & Akiyoshi, K. Self-assembled polysaccharide nanogel delivery system for overcoming tumor immune resistance. *J. Control Release* **347**, 175–182 (2022).
41. Ishihara, M. et al. NY-ESO-1-specific redirected T cells with endogenous TCR knockdown mediate tumor response and cytokine release syndrome. *J. Immunother. Cancer* **10**, e003811 (2022).
42. Miyauchi, K. et al. Clinical relevance of antigen spreading pattern induced by CHP-MAGE-A4 cancer vaccination. *Immunotherapy* **8**, 527–540 (2016).
43. Kageyama, S. et al. Dose-dependent effects of NY-ESO-1 protein vaccine complexed with cholesteryl pullulan (CHP-NY-ESO-1) on immune responses and survival benefits of esophageal cancer patients. *J. Transl. Med.* **11**, 246 (2013).
44. Nagata, Y. et al. Prognostic significance of NY-ESO-1 antigen and PIGR expression in esophageal tumors of CHP-NY-ESO-1-vaccinated patients as adjuvant therapy. *Cancer Immunol. Immunother.* **71**, 2743–2755 (2022).
45. Kang, Y. S. et al. SIGN-R1, a novel C-type lectin expressed by marginal zone macrophages in spleen, mediates uptake of the polysaccharide dextran. *Int. Immunol.* **15**, 177–186 (2003).
46. Krummey, S. M. et al. CD45RB Status of CD8(+) T cell memory defines T cell receptor affinity and persistence. *Cell Rep.* **30**, 1282–1291 e1285 (2020).

47. Winkler, E. S. et al. SARS-CoV-2 infection of human ACE2-transgenic mice causes severe lung inflammation and impaired function. *Nat. Immunol.* **21**, 1327–1335 (2020).
48. Zafarani, A. et al. Natural killer cells in COVID-19: from infection, to vaccination and therapy. *Future Virol.* **18**, 177–191 (2023).
49. Fischer, D. S., Wu, Y., Schubert, B. & Theis, F. J. Predicting antigen specificity of single T cells based on TCR CDR3 regions. *Mol. Syst. Biol.* **16**, e9416 (2020).
50. Thomas, N. et al. Tracking global changes induced in the CD4 T-cell receptor repertoire by immunization with a complex antigen using short stretches of CDR3 protein sequence. *Bioinformatics* **30**, 3181–3188 (2014).
51. Burgdorf, S., Lukacs-Kornek, V. & Kurts, C. The mannose receptor mediates uptake of soluble but not of cell-associated antigen for cross-presentation. *J. Immunol.* **176**, 6770–6776 (2006).
52. Burgdorf, S., Kautz, A., Bohnert, V., Knolle, P. A. & Kurts, C. Distinct pathways of antigen uptake and intracellular routing in CD4 and CD8 T cell activation. *Science* **316**, 612–616 (2007).
53. Sancho, D. et al. Identification of a dendritic cell receptor that couples sensing of necrosis to immunity. *Nature* **458**, 899–903 (2009).
54. Joffre, O. P., Segura, E., Savina, A. & Amigorena, S. Cross-presentation by dendritic cells. *Nat. Rev. Immunol.* **12**, 557–569 (2012).
55. Engering, A. et al. The dendritic cell-specific adhesion receptor DC-SIGN internalizes antigen for presentation to T cells. *J. Immunol.* **168**, 2118–2126 (2002).
56. Granelli-Piperno, A. et al. Dendritic cell-specific intercellular adhesion molecule 3-grabbing nonintegrin/CD209 is abundant on macrophages in the normal human lymph node and is not required for dendritic cell stimulation of the mixed leukocyte reaction. *J. Immunol.* **175**, 4265–4273 (2005).
57. Cannon, M. J., Openshaw, P. J. & Askonas, B. A. Cytotoxic T cells clear virus but augment lung pathology in mice infected with respiratory syncytial virus. *J. Exp. Med.* **168**, 1163–1168 (1988).
58. Machhi, J. et al. The natural history, pathobiology, and clinical manifestations of SARS-CoV-2 infections. *J. Neuroimmune Pharm.* **15**, 359–386 (2020).
59. Mayer-Blackwell, K. et al. TCR meta-clonotypes for biomarker discovery with tcrdist3 enabled identification of public, HLA-restricted clusters of SARS-CoV-2 TCRs. *Elife* **10**, e68605 (2021).
60. Chang, C. M. et al. Profiling of T cell repertoire in SARS-CoV-2-infected COVID-19 patients between mild disease and pneumonia. *J. Clin. Immunol.* **41**, 1131–1145 (2021).
61. Pan, Y. G. et al. Vaccination reshapes the virus-specific T cell repertoire in unexposed adults. *Immunity* **54**, 1245–1256 e1245 (2021).
62. Hanson, H. L. et al. Eradication of established tumors by CD8+ T cell adoptive immunotherapy. *Immunity* **13**, 265–276 (2000).
63. Muraoka, D. et al. Establishment of animal models to analyze the kinetics and distribution of human tumor antigen-specific CD8(+) T cells. *Vaccine* **31**, 2110–2118 (2013).
64. Wikramaratna, P. S., Paton, R. S., Ghafari, M. & Lourenco, J. Estimating the false-negative test probability of SARS-CoV-2 by RT-PCR. *Euro Surveill.* **25**, 2000568 (2020).
65. Corman, V. M. et al. Detection of 2019 novel coronavirus (2019-nCoV) by real-time RT-PCR. *Euro Surveill.* **25**, 2000045 (2020).
66. Kitaura, K., Shini, T., Matsutani, T. & Suzuki, R. A new high-throughput sequencing method for determining diversity and similarity of T cell receptor (TCR) alpha and beta repertoires and identifying potential new invariant TCR alpha chains. *BMC Immunol.* **17**, 38 (2016).
67. Kitaura, K. et al. Different somatic hypermutation levels among antibody subclasses disclosed by a new next-generation sequencing-based antibody repertoire analysis. *Front Immunol.* **8**, 389 (2017).
68. Chen, Z. et al. Inference of immune cell composition on the expression profiles of mouse tissue. *Sci. Rep.* **7**, 40508 (2017).

Acknowledgements

We thank Yamaguchi Sayuri, Akane Katagiri, Minami Isaka, Kirara Iwanaga, Kazumi Haga, Rieko Haraguchi, and Shashika Lavangi Wijesooriya; members of the Department of Virology, Institute of Tropical Medicine, Nagasaki University; members of the Department of Developmental Medicine, Graduate School of Medicine, University of Tokyo; and staff of United Immunity and Repertoire Genesis Ltd. for providing technical assistance, advice, and support. We would like to acknowledge Drs. Makoto Takeda, Masayuki Saijo, and Mutsuo Ito of the National Institute of Infectious Diseases, Japan, for providing the SARS-CoV-2 strain (2019-nCoV/Japan/TY/WK-521/2020). We would also like to express our deepest gratitude to Drs. Koichi Morita and Ngwe Tun Mya Myat of Nagasaki University for assistance in the use of the animal facility regarding the SARS-CoV-2 animal experiments. This study was supported by Japan Agency for Medical Researchs and Development under grant number JP20pc0101048, JP21wm0125006, and JP223fa627001 to M.L.M. or N.H., and 243fa727001h0003 to K.A.

Author contributions

D.M. and M.L.M. designed the experiments; D.M., M.L.M., T.N., S.D., C.T., H.H., Y.H., N.H., and T.T.N.N. performed the experiments; D.M. analyzed the data; M.L.M., N.H., T.S., S.S., N.T.M.M., K.A., H.M., T.N., and H.I. contributed reagents, materials, and analytical tools; O.M. and R.Y. analyzed the TCR-seq data; D.M., M.L.M., O.M., and N.H. wrote the original draft of the paper; all authors approved the final draft for journal submission.

Competing interests

Y.H., T.S., and N.H. is an employee, Chief Scientific Officer, and Chairman of United Immunity, Co., Ltd., respectively. The other authors declare no conflicts of interest.

Additional information

Supplementary information The online version contains supplementary material available at https://doi.org/10.1038/s41541-024-00961-6.

Correspondence and requests for materials should be addressed to Daisuke Muraoka or Meng Ling Moi.